5

Remaining Issues in Upper Atmosphere Satellite Drag

Jeffrey P. Thayer[1], **W. Kent Tobiska**[2], **Marcin D. Pilinski**[3], **and Eric K. Sutton**[4]

ABSTRACT

The greatest concentration of spacecraft and space debris resides in an orbital band between 100 and 2000 km altitude, classified as low-Earth orbit (LEO). Of these space objects, those below about 1000 km all experience an appreciable drag force due to the presence of Earth's atmosphere. It has been a common approach to use LEO spacecraft orbital behavior to extract upper atmosphere properties and then reapply this atmosphere description to predict future spacecraft behavior using orbit propagators. This approach leads to mutual coupling between spacecraft response and atmosphere change that results in convoluted uncertainties. To unravel such interdependencies, a physical description of the LEO space environment and how it changes due to external influences is required independently of the physical description for atmosphere-spacecraft interactions. The main challenge lies in attributing how much of the orbital perturbation is the result of changes in the upper atmosphere versus changes in a satellite's ballistic coefficient. Today, greater fidelity in space environment specification is required for LEO spacecraft operations, collision avoidance procedures, and space environment forecasting. This chapter highlights the remaining issues by segmenting the LEO drag environment into a lower and upper register, and describing separately the LEO environment and gas-surface interaction in each register. In addition, advances in solar and geomagnetic drivers for improved density specification are described.

5.1. INTRODUCTION

Upper atmospheric drag represents a scientific, engineering, and societal issue where spacecraft in low-Earth orbit (LEO) experience uncertain and variable forces due to rapid and appreciable changes in the rarefied gas. These upper atmosphere changes are challenging to describe and to predict, requiring LEO operating spacecraft to be regularly monitored. The LEO domain is popular among satellite providers as it gives access to space operations using only modest launch capability, provides remote sensing of Earth at high spatial resolution, gives astrophysical instruments an unobstructed view of space void of atmospheric distortion and absorption, and offers a set of orbits known as sun-synchronous repeat orbits that provide a near-constant alignment of the orbital plane and the projected direction of the Sun, giving optimum and repeatable illumination conditions for imaging Earth's surface.

---

[1] *Ann and H. J. Smead Aerospace Engineering Sciences Department, University of Colorado at Boulder, Boulder, Colorado, USA*

[2] *Space Environment Technologies, Pacific Palisades, California, USA*

[3] *Laboratory for Atmospheric and Space Physics, University of Colorado at Boulder, Boulder, Colorado, USA*

[4] *Space Weather Technology, Research, and Education Center, University of Colorado at Boulder, Boulder, Colorado, USA*

Space Physics and Aeronomy Collection Volume 5: Space Weather Effects and Applications, Geophysical Monograph 262, First Edition.
Edited by Anthea J. Coster, Philip J. Erickson, and Louis J. Lanzerotti.

DOI: 10.1002/9781119815600.ch5

The public expectation of uninterrupted satellite services with sustained high-fidelity performance is a constant challenge for operators of LEO spacecraft, not to mention the human spaceflight activity in this domain. The variable atmospheric drag forces and torques on the spacecraft can alter its orbit and attitude. Furthermore, a continuous account must be made of the large population of space objects (also altered by atmospheric drag) that includes over 17,000 objects larger than 10 cm and growing. Today, the LEO domain, often defined between 100 and 2000 km, contains almost 74% of the on-orbit catalog population and 34% of its overall mass in just 0.4% of the volume extending from the Earth's surface to geostationary orbit (Klinkrad, 2017). A new addition to LEO activity is the planned large satellite constellations, or *megaconstellations*, promising continuous, global communication and internet services. Such proposed constellations in LEO include SpaceX with 4000 satellites, Samsung with 4200 satellites, and OneWeb with 720 satellites (Radtke et al., 2017). The benefit of operating at lower altitudes is the much lower signal delay times and less power required to transmit a signal. However, operating in this altitude range requires a considerable number of satellites to provide complete on-ground coverage. The presence of the megaconstellation in LEO makes the need for detailed descriptions of the LEO environment even more critical.

Upper atmosphere drag involves the behavior of a multiconstituent rarefied gas in the thermosphere and exosphere, and its interaction with the surfaces of resident space objects in LEO. This interaction represents the largest nongravitational perturbation to Keplerian orbits below approximately 500 km altitude, causing an overall decrease in orbital energy and decaying the orbit towards re-entry. At LEO altitudes, satellite drag is the most variable orbital perturbation and the one that is the most difficult to predict. To fully account for and predict atmospheric drag perturbations on LEO objects, a physical description of the global gas state and the spacecraft's gas-surface interaction is required. The requirements for satellite drag modeling have become more acute as the LEO object population continues to increase; the current, and future, situation requires continuous precise orbit determination, conjunction assessment, and collision avoidance actions that involve not only the spacecraft response to atmospheric drag but the drag response of all the other space objects in or passing through LEO. Inherently, there are errors in the system that make the position of space objects uncertain, and these uncertainties become cumulative when trying to predict an object's future position and velocity in a changing atmosphere environment. Atmospheric drag in LEO is highly dependent on the state of the neutral gas population that makes up the Earth's thermospheric/exospheric mass density (100–1000 km altitude). It has been well established that atmospheric drag, and in particular variability in atmospheric neutral density, is the primary error source for LEO objects (Bowman, Tobiska, Marcos, Huang, et al., 2008; Hejduk & Snow, 2018; Storz et al., 2005). Thus, improved estimates of atmospheric density will positively impact the operations and performance of these critical space assets. Space weather events, and longer-term space climate, can alter the state of the upper atmosphere and produce variability that can exceed several hundred percent of the mean state at some LEO altitudes. Figure 5.1 illustrates the major pathways by which space weather couples to the upper atmosphere, leading to changes in upper atmosphere gas properties, impacting the forces on the satellite, and resulting in the assessment of orbital properties.

The magnitude of satellite drag forces is proportional to the gas mass density and the square of the magnitude of relative velocity between the satellite and the atmosphere. The drag experienced by an orbiting object also depends on the satellite area, the shape of the satellite, the temperature and composition of the atmosphere, the atmosphere mean-free path relative to the size of the satellite, and the scattering dynamics of atmospheric molecules from the spacecraft surfaces. Scattering dynamics stochastically describe the velocity, energy, and momentum of molecules scattered from the surface and are themselves a function of incident molecular energy, incident angle, composition, and a variety of surface properties. These properties (area, shape, etc.) are often subsumed in an object's ballistic coefficient, essentially a sensitivity factor unique to each space object that gauges the level of responsivity of the space object to a change in density and/or relative velocity. The challenge lies in the interdependencies that exist between the changes in the state of the space environment that directly impact drag accelerations and indirectly affect the ballistic coefficient. Thus, the net drag acceleration depends on the state of the space environment and the sensitivity of the space object response to changes in that state.

The following sections address remaining issues in the LEO drag environment, specified here to be the region where atmosphere drag has an appreciable influence on satellites, from 100 to 1000 km. Section 5.2 provides background information and places in context some current capabilities while expressing the societal need for more research. Section 5.3 addresses the physics behind the LEO drag problem and establishes two specific registers within the LEO drag environment: lower (100–500 km) and upper (500–1000 km), where the physics of the problem differs. Section 5.4 covers the lower register and the issues related to rarefied gas dynamics treated as a

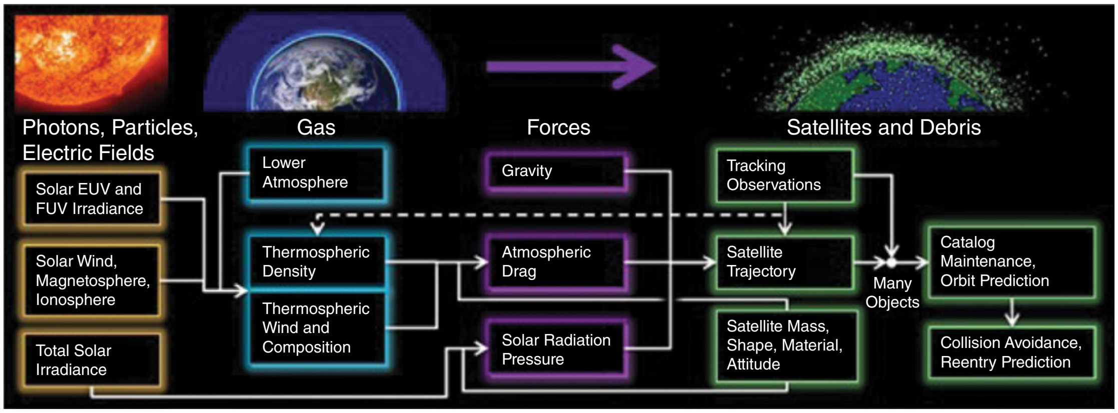

Figure 5.1 Major pathways by which space weather couples to satellite aerodynamic forces. (Source: J. Emmert, NRL.)

continuum and gas-surface interactions under free molecular flow with high accommodation. Section 5.5 covers the upper register and the issues related to rarefied gas dynamics transitioning from a continuum to a kinetic regime, and gas-surface interactions transitioning from an oxygen to a helium and hydrogen environment with low accommodation. Section 5.6 addresses the significant advancements in the last 40 years related to the improvement of density specification from solar and geomagnetic drivers.

5.2. BACKGROUND

Since the beginning of the space age, atmospheric drag has been studied to discern its impact on LEO objects. Observations of changes in LEO objects have revealed large-scale, long-term behavior in upper atmosphere density (e.g. King-Hele & Quinn, 1965). It has been a common approach to use observed changes in LEO spacecraft orbits as instruments for estimating space environment properties, particularly gas mass density and winds, by assuming knowledge, or stability, of the ballistic coefficient. The ballistic coefficient assumptions made when constructing or calibrating atmospheric models based on orbital observations are implicitly entered into those descriptions of the atmospheric mass density. This derived description of the space environment is then reapplied to space objects for nowcasting and forecasting behavior using spacecraft orbit propagators. A "fitted" ballistic coefficient is often computed as part of this process since the ballistic coefficient assumptions made in constructing/calibrating any given atmospheric model are usually not known to the model user (e.g. Hoots & Roehrich, 1980; Gaposchkin & Coster, 1988; Marcos et al., 1998; Storz et al., 2005; Vallado et al., 2006). To determine a fitted coefficient, empirical or physics-based descriptions of the LEO space environment are assumed to be "known" properties to solve for the most recent ballistic coefficient given the observed drag acceleration. These observations, along with others of varying degrees of direct thermosphere state specification, have led to the development of empirical models. Emmert (2015) has provided an extensive review of approaches to describe and observe thermosphere mass density spanning the period from 2000 to 2014 and identified mass density features that have been elucidated using these various approaches over the prescribed time span. The approaches described cover measuring techniques, empirical models that provide a synthesis of historical data, and physical models that simulate the environment by solving fluid equations. Figure 5.2 provides a climatological view of the thermosphere state as described by NRLMSISE-00® empirical model (shortened to MSIS; Picone et al., 2002). The largest uncertainties driving change to this climatological view of the LEO drag environment are solar, lower atmosphere, and geomagnetic drivers. Progress to date in solar and geomagnetic drivers for the LEO drag environment is discussed in section 5.6.

He et al. (2018) have also assessed several empirical/semiempirical thermosphere models to assess their ability to reproduce spatial variations and their ability to capture complex features in thermosphere mass density. The models included the Jacchia model (Jacchia, 1977), High Accuracy Satellite Drag Model (HASDM; Storz et al., 2005), MSIS, Jacchia-Bowman (JB2008; Bowman, Tobiska, Marcos, Huang, et al., 2008), Drag Temperature Model (DTM-2013; Bruinsma, 2015), and Global Average Mass Density Model (GAMDM; Emmert et al., 2008). The ISO International Standard 14222 on Earth's upper atmosphere (2013) recommends using

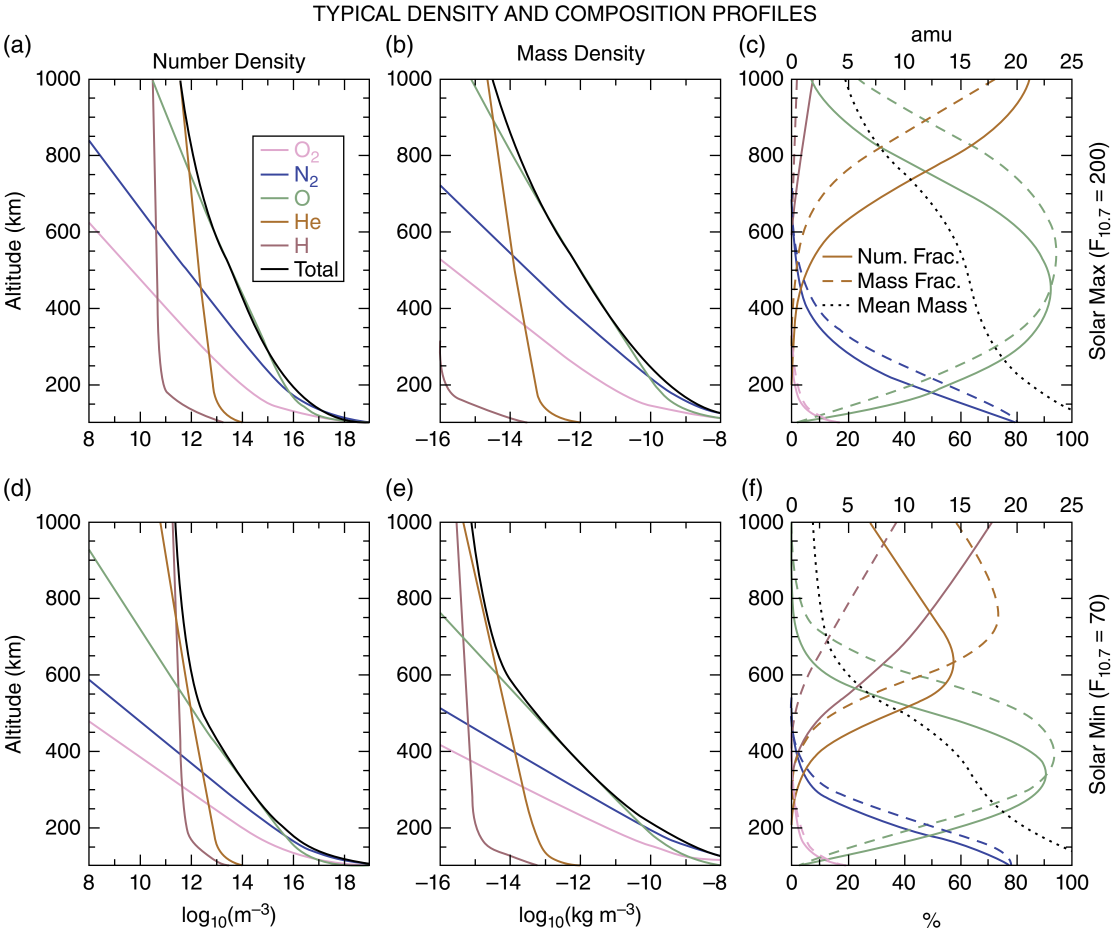

Figure 5.2 (a) Global average number density profiles at solar maximum ($F_{10.7}$ = 200 solar flux units [1 sfu = 10^{-22} W m^{-2} Hz^{-1}]) from the NRLMSISE-00® empirical model. Shown are profiles of O_2 (purple), N_2 (blue), O (green), He (orange), H (red), and the total number density (black). (b) Corresponding mass density profiles for each species. (c) Number mixing ratios (solid lines) and mass mixing ratios (dashed lines) for each species. Also shown is the mean molecular mass in atomic mass units (dotted black line), referenced to the upper axis of the plot. (d)–(f) Same as (a)–(c), but for solar minimum ($F_{10.7}$ = 70) conditions. (Source: Emmert, 2015. Reproduced with permission of Elsevier.)

MSIS for relative constituent abundances and JB2008 for mass densities related to satellite drag. Marcos et al. (2006) led the first conclusive studies that identified the Jacchia-Bowman series of models, starting with JB2006, as the most significant advance in empirical modeling since the 1960s. This was due to several factors, including the use of three new solar indices and proxies tying source regions on the Sun to energy absorption and species altitudes in the Earth's upper atmosphere (removing the dependence on the F10.7 proxy), the use of Dst as a geomagnetic driver during storm periods (removing the dependence on the Ap proxy), and the inclusion of semiannual hemispheric variability. In JB2008, the 1-sigma uncertainties at 400 km for a given epoch dropped from 15% to 8% compared with Jacchia and MSIS models. The use of JB2008 in HASDM, and the assimilation of calibration satellite data into the initial JB2008 density solutions, further dropped the comparable HASDM density uncertainties to less than 5%.

HASDM has the unique quality of including calibration satellites to solve for thermospheric neutral density in near real time by incorporating the observed drag effects on a set of low-perigee inactive payloads and debris. Many different calibration satellites with different orbits may be exploited to recover a dynamically varying global density field. The greater the number of calibration satellites, the better the accuracy. Typically, 75 calibration satellites are used. HASDM is an example of a type of data/model assimilation. This method improves the accuracy of current epoch and near-term parameters compared to modeling alone. Because HASDM is able to mitigate uncertainty in atmosphere effects at each epoch, by resolving the differences between calibration satellites and the core JB2008 model, real-time nowcasting specification of the LEO drag environment has improved significantly. Forecasting is then achieved with the JB2008 model, driven by the solar and geomagnetic drivers described in section 6, with uncertainties growing significantly a few hours postepoch. The calibration satellites operated by the Air Force are regularly monitored for changes in their orbital properties, and a subset of objects are replaced on an annual basis. The HASDM results are then implemented into orbit propagators for all other space assets.

In more recent times with the advancement of scientific-grade accelerometers sensitive to nano-G forces, the LEO spacecraft has become a refined instrument for deriving high-resolution behavior in thermosphere neutral mass density and neutral winds. This approach has been profoundly demonstrated by the CHAMP and GRACE missions (Doornbos et al., 2010; Sutton, 2008; Sutton et al., 2007). (The GOCE mission also provided unprecedented sensitivity for mass density and winds but performed such precision through sensitive thruster operations to create a free-flying spacecraft at altitudes near 250 km.) These available data sets have led to improvements in empirical and physics-based models, either as a data source or a validation procedure. Recent work by Mehta and Linares (2017) invokes techniques to exploit the capabilities of both empirical and physics-based models using proper orthogonal decomposition. High-resolution GPS data from LEO spacecraft have also been introduced as a means to extract density using GPS accelerometry (van den IJssel & Visser, 2010) at a time cadence higher than conventional ground-based tracking approaches can provide but lower than high-precision accelerometers (Ren et al., 2018).

The increasing congestion of the space environment is well known even outside of the space industry. Figure 5.3 provides a current and future snapshot of LEO objects provided by The Aerospace Corporation. Allowed to continue unabated, increases in space debris will eventually prevent the most useful Earth orbital bands from being safely occupied, thus threatening the commercial, civil, and military uses of space on which modern society relies. The emerging approach to remediation involves both reducing existing space debris (active debris removal) and preventing future debris-producing events (conjunction assessment and collision avoidance operations). Conjunction assessment is the process of determining close approaches between two objects, assessing the probability of collision, and providing this information to satellite owners/operators (Hejduk & Snow, 2018). Collision avoidance involves weighing the risk posed by the close

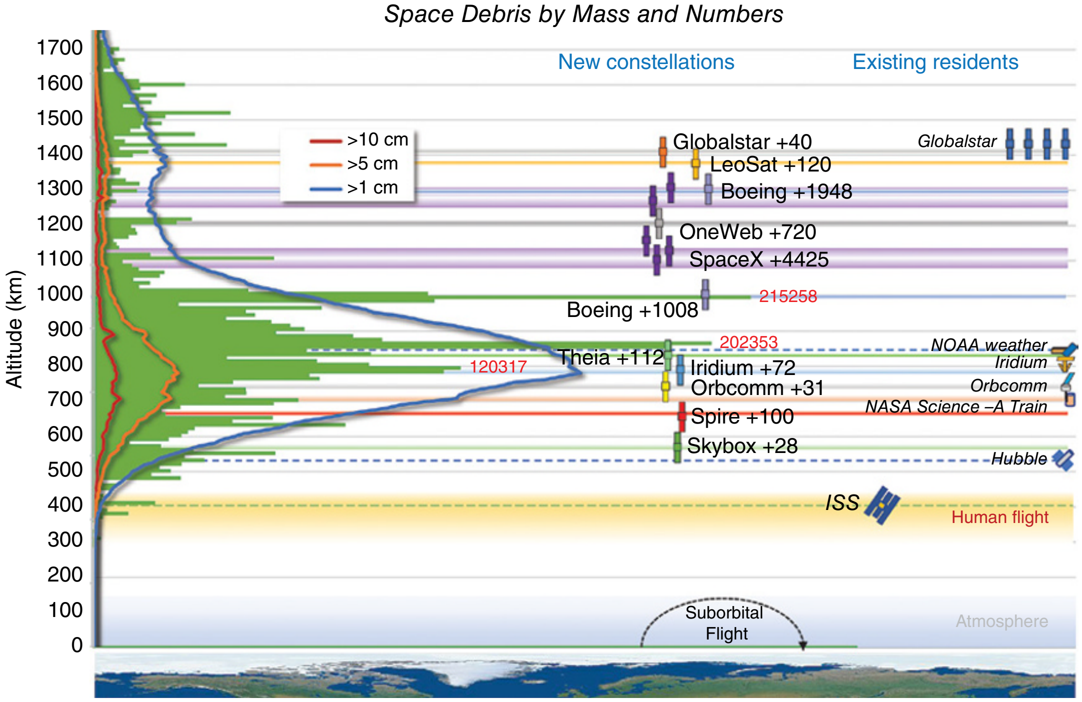

Figure 5.3 LEO object population densities and future potential constellations. (Source: Dr. Ted Muelhaupt of Aerospace Corporation.)

approach against the cost and risk of a maneuver. The latter used to be practiced only to protect high-value space assets from a catastrophic collision that would prematurely end its mission life. Today, conjunction risk assessment and remediation activities are seen as necessary to preserve the space environment for all space assets (Hejduk & Snow, 2018; Bussy-Virat et al., 2018).

Industry has embraced the probability of collision (Pc) as the standard parameter for conjunction risk assessment; to calculate this parameter requires state estimates of the two satellites and estimates of the uncertainties at the time of the satellites' closest approach. The greatest encumbrance to accurate Pc calculations today is the lack of reliable estimates of atmospheric drag and, at least as important, a reliable quantification of the uncertainty of the drag estimates that are produced. Drag variability produces position errors for both satellites. These errors change the time of closest approach, which in turn can often change the Pc severely enough to cause the event to be incorrectly categorized (i.e. as not high risk when it is in fact high risk). Because the Pc calculation considers the estimation errors as part of the calculation, an accurate atmospheric drag error estimate can increase or decrease the conjunction risk depending on the quality of the atmospheric density determination.

A highly accurate calculation of Pc is important because remediation efforts must be reserved for only the most risky conjunctions. The growing debris environment now produces so many conjunction notifications that individual attention and remediation planning can be given only to those events with the highest Pc. The SOCRATES (Satellite Orbital Conjunction Reports Assessing Threatening Encounters in Space) program at the Center for Space Standards and Innovation screens 3,541 primaries each day against a total of 15,084 objects (David Vallado, personal communication). It typically finds over 18,000 conjunctions within 5 km for the coming 7 days. NASA receives over 800 per day for the suite of satellites they protect. Because Pc is the gatekeeper for remediation consideration, safety of flight in LEO will benefit enormously from improved accuracy and error quantification of drag.

Inherent to any spacecraft operation is the maintenance/control of attitude and orbit that meet the requirements of the on-board technology. Satellite remote sensing is especially dependent on such operations. Improvements in drag estimation optimize the maneuvers that keep a spacecraft in its control box. Re-entry of space objects is also of major concern. Uncontrolled reentries (UARS, ROSAT, Phobos-Grunt, and GOCE satellites) are of particular concern and require accurate estimates of atmospheric mass density to predict the time and place of surface impact. Estimated times of reentry typically span roughly a week with +/- 3-day accuracy, and the estimated area of impact is often described to occur over broad regions of Earth. Improved estimates of the atmospheric drag environment would significantly improve re-entry predictions.

Various forms of energy from space weather drivers (solar soft X-ray [XUV], extreme ultraviolet [EUV], and far ultraviolet [FUV] flux, including the temporal effects of solar flares, coronal mass ejections, and corotating interaction regions) and lower atmosphere events (gravity, planetary, and tidal wave propagation) significantly perturb the upper atmosphere state over a variety of temporal and spatial scales. The broad range of external forcing on the upper atmosphere and its variability results in a highly dynamic, continuously changing state. These energy inputs and subsequent processes need to be adequately represented and are required for the assessment of physics-based models under different influences of space weather and lower atmosphere events. Physics-based models used for data–model comparisons include the Thermosphere-Ionosphere-Electrodynamics General Circulation Model (TIE-GCM; Richmond et al., 1992; Roble et al., 1988), Coupled Thermosphere-Ionosphere-Plasmasphere electrodynamics model (CTIPe; Fuller-Rowell et al., 1996), and the Global Ionosphere-Thermosphere Model (GITM; Ridley et al., 2006); see Emmert (2015) for more details.

The pathway for ensuring continuous and secure operations of LEO spacecraft technology is to improve the estimate of the upper atmosphere state and predict its response to space weather events. To do so requires advancements in modeling upper atmosphere gas behavior as well as a predictive capability for solar and geomagnetic drivers. Since 2001 there has been significant progress in improving estimates and advancing models of atmospheric mass density in the lower register of the thermosphere (100–500 km altitude), but further work is needed in this altitude range. Gas composition measurements are critically important, as they constitute the total mass density and how the mass density will respond to heating events. Composition also impacts the manner by which gas-surface interactions evolve. Thermosphere temperature is also critically important for describing gas behavior and impact on spacecraft, and significant advancements could be made with regular and extensive coverage of simultaneous measurements of global composition and temperature. Such measurements have not been made since the early 1980s, resulting in reliance on climatological descriptions of temperature and composition that simply do not capture the variability or correlated activity necessary to describe the current or future state of the upper atmosphere.

A key deficiency that requires much more investigation is nowcasting and predicting atmospheric drag in the upper register of the LEO drag environment (500–1000 km altitude). In fact, atmospheric drag estimates are more coveted by operators in this domain than at lower altitudes because of the larger number of operational space assets and debris (see Figure 5.3). For upper atmosphere research, this altitude domain includes the challenging transition from gas continuum to particle dynamics, as the thermosphere gives way to the exosphere and is highly sensitive to space weather and the changing boundary conditions imposed by the underlying layers. For the engineering community, the diverse and dynamic population of light ion and neutral constituents in this altitude range makes estimation of spacecraft drag coefficients especially challenging. Finally, for the operator community, conjunction assessment and collision avoidance are daily issues in this LEO altitude range. Improvements in nowcasting and forecasting atmospheric drag in the lower register will be important for expanding the models into the higher register, making the 500–1000 km altitude range particularly challenging and in need of improvements in all aspects of the atmospheric drag problem.

5.3. THE PHYSICS OF ATMOSPHERIC DRAG ON SPACECRAFT

The physics of atmospheric drag on spacecraft has similarities to atmospheric drag described by low-speed aerodynamicists on aircraft in that forces exerted on the body in a moving gas produce a drag force defined to be parallel to the velocity of the gas relative to the body. The projected aerodynamic forces in the drag direction produce a scalar force per unit mass, or drag acceleration, on the body that is proportional to the dynamic pressure of the gas. A proportionality factor, B, can be applied such that the drag acceleration is

$$a_D = B\frac{1}{2}\rho v_r^2. \tag{5.1}$$

This illustrates that the value of B or its inverse, often called the ballistic coefficient parameter b, represents a measure of sensitivity for a body to be perturbed by the dynamic pressure of the gas. It is common to apply dimensional analysis to express B in terms of a drag coefficient, C_D, multiplied by an area-to-mass ratio, and express the drag acceleration as

$$a_D = C_D\frac{A_{ref}}{m}\frac{1}{2}\rho v_r^2. \tag{5.2}$$

Here A_{ref} is more generally expressed as a reference area of the body, m is the mass of the body, ρ is the mass density of the gas, and v_r is the velocity of the gas relative to the body. The reference area is a value assigned to represent the cross-sectional footprint of the satellite in the plane normal to v_r. The mass represents that of the entire spacecraft including fuel. The mass density is that of the multiconstituent, rarefied upper atmosphere gas. The relative velocity is the vector addition of the inertial velocity of the spacecraft, the inertial velocity of the corotating atmosphere, and the velocity due to winds in an Earth-fixed atmosphere. Accounting for signs, the velocity of the gas relative to the body, v_r, is $-(v_{sat} - v_{corot} - v_{wind})$, where the outside negative sign indicates that the relative velocity is opposite to the body velocity. The corotation and wind velocities represent the bulk velocity of the gas, but thermal motion of the gas particles may also need to be included when considering atmospheric drag in LEO. This thermal component is often accounted for in the estimate of the C_D and becomes particularly important for spacecraft bodies with elongated surfaces and high-altitude portions of LEO orbits (Sutton, 2009).

Much of the physics of the gas and body interaction is contained within the nondimensional drag coefficient and, for continuum aerodynamics, is often experimentally retrieved by performing a series of wind tunnel tests that measure the drag force with all other properties known. This is not viable for bodies in space and, furthermore, the physics of the gas and body interaction in LEO is quite different than for the troposphere and aircraft. Consequently, various modeling and measurement approaches are employed to estimate C_D, or the combined ballistic coefficient, while in orbit. Often, spacecraft are modeled as surface segments by which individual drag coefficients are determined and then summed to determine the total drag coefficient of the spacecraft (Pilinski & Argrow, 2013). Furthermore, the individual species of the thermosphere interact differently with the spacecraft surface and should be addressed separately, and these accumulated effects are captured in a mass-weighted sum. Thus, gas-surface interactions must be properly defined and physically accurate to describe spacecraft drag.

A common physical description for the upper atmosphere gas employs continuum gas dynamics, where average values of macroscopic upper atmosphere properties are determined and predicted with appropriately justified mathematical models for describing the conservation of mass, momentum, and energy of the gas within the LEO environment. The reason for the continuum mechanics in this context is that the mean free paths, while large relative to the size of a satellite, are much smaller than the characteristic size of most atmospheric features. Such continuum atmospheric models provide a total mass density and mass-averaged wind globally, among many other properties, that can be applied to equation (5.2). Gas-surface interactions invoke a different physical description where

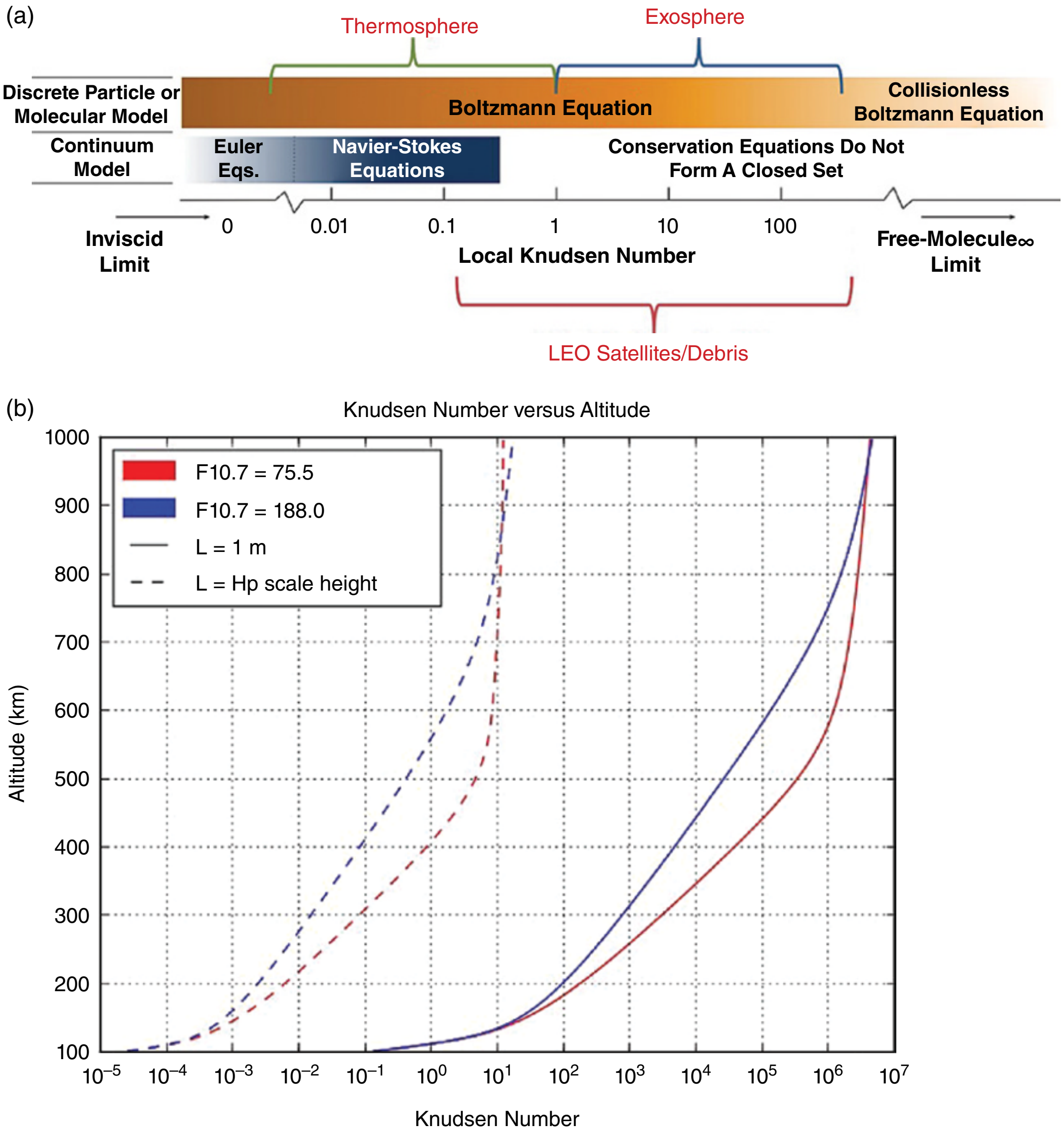

Figure 5.4 (a) Flow regimes according to the Knudsen number for gas dynamics and gas-surface interactions (adopted from Bird, 1994). (b) The graph indicates the Knudsen number for a 1-meter spacecraft (solid line) and for atmospheric gas behavior using density scale height (H_p) as a representative scale length under solar maximum and minimum conditions. (Source: Bird, 1994. Reproduced with permission of Oxford University Press.)

microscopic properties of the gas are needed to account for the energy and momentum exchange between the gas particles and the spacecraft surface. In this case, gas kinetic theory is the more appropriate framework by which the drag coefficient can be modeled.

Figure 5.4 summarizes the physical description of these two different aspects to atmospheric drag (upper atmosphere gas description and gas-surface interactions) in terms of the Knudsen number. The Knudsen number (Kn) is the ratio of the mean free path between collisions to a representative gradient scale length of the gas, or scale length of a body, and is a useful dimensionless number to evaluate approximations to gas flow regimes. For Kn less than 1, the gas is adequately described by continuum gas dynamics. For Kn greater than 1, the gas description requires more sophistication, and above about 10 a particle trajectory approach employing gas kinetics must be applied (Bird, 1994). The Knudsen number for describing the thermosphere gas mathematically using transport equations relates the mean free path (determined using MSIS and hard-sphere, neutral-neutral collisions) to the scale length of the macroscopic gradient in mass density, considered as the absolute value of the density scale height, $H_p = -\rho/(d\rho/dz)$, also determined using MSIS. This is displayed as an altitude plot versus Knudsen number. A value of $Kn < 0.1$ satisfies the application of Navier-Stokes equations to the thermosphere gas (i.e. continuum aerodynamics). Often, $Kn = 1$ is used to indicate the transition between the thermosphere and the exosphere, or the exobase, but this transition is a more extended domain where further approximations to the heat flux vector and momentum flux tensors could be required before ultimately replacing the continuum mathematical model with collision-less gas kinetic theory ($Kn > 10$).

There are several scenarios where the Knudsen number can exceed 1 in describing a gas. One is at the point where gradients in gas variables become so steep that smaller and smaller volumes of the flow are required to describe its characteristics. In this case, one must consider whether there are a sufficient number of molecules or atoms within the volume to appropriately describe the gas macroscopic properties. In other words, the gradients of the macroscopic properties become so steep that their scale length is of the same order as the average distance traveled by the molecules and atoms between collisions. This can occur in regions of shocks or sharp boundaries. Another case is where the gradients are sufficiently large but the gas becomes so tenuous that the mean free path exceeds the gradient scale. This is commonly experienced in transitioning from the thermosphere to exosphere, and the gas must be treated more by its free molecular flow than by its continuum flow. For the entire LEO domain, the upper atmosphere gas description will need to span continuum and free molecular flow regimes.

The Knudsen number for gas-surface interactions of a spacecraft with a physical dimension of 1 meter versus altitude is also plotted in Figure 5.4, again using MSIS to determine the mean free path. Here it is clear that values exceed 1 in the lower thermosphere and that LEO objects are generally in the free-molecular flow regime for most of the thermosphere and above. Under this flow condition the probability that two molecular collisions occur simultaneously is very small. Furthermore, it is assumed the incident and reflected molecules do not interact with each other near the surface (see Sentman 1961b, section V.A). The dynamical processes reduce to addressing the successive collisions among a gas atom/molecule and the object. It is in this regime of free-molecular flow that gas-surface interactions are modeled and used in estimating the drag coefficient of the spacecraft.

In the early stages of the space age, a judicious selection of a constant drag coefficient value of 2.2 was employed to carry out many calculations of upper atmosphere density behavior derived from orbit decay. It was recognized then that this value will likely vary over altitude and geophysical conditions (Cook, 1965), but the required precision was not as stringent as it is today. An example of drag coefficient variability is shown in Figure 5.5, where a SL6 cylindrical rocket body (satellite 16125) shows clear change in the drag coefficient derived from the ballistic coefficient (black triangles) as the

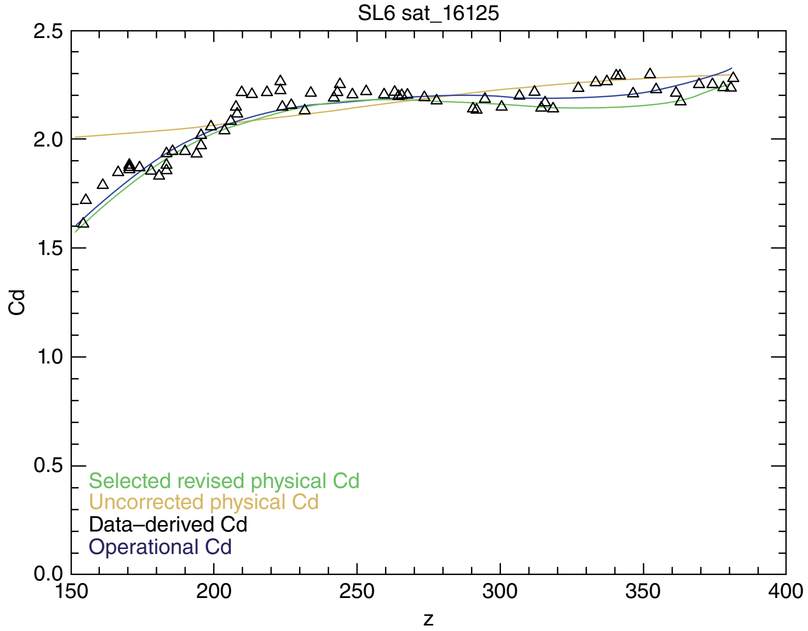

Figure 5.5 The altitude-variable drag coefficient for a SL6 cylindrical rocket body (satellite 16125) that changed from 2.3 to 1.5 as the object moved through atmosphere regimes with different species compositions. (Source: Tobiska and Bowman, unpublished work.)

altitude changes from an atomic oxygen region above 200 km to a mixed atmosphere below 200 km. The maximum C_D was 2.3 and the minimum was 1.5. In this figure, polynomial fits to the data are shown using assumptions of corrections to a physical C_D in the green line (Moe & Moe, 2005), an uncorrected physical C_D as the gold line, and a predicted C_D for operational purposes as the blue line.

Thus, density models derived from such observations inherently include uncertainties introduced by the lack of accuracy in the drag coefficient. As in any collisional exchange, the fundamental issue in describing the drag coefficient resides in the manner by which momentum and energy are exchanged through the interaction process. More specifically, account must be made of how momentum and kinetic energy of the gas changes when interacting with the satellite body. Analytical solutions of free molecular flow for simple shapes have had an extensive history, and a review of these techniques was recently given by Prieto et al. (2014). The force per unit area on the satellite surface is equal to the change in the momentum flux of the incident and reflected gas. Descriptions for the incident momentum flux have been organized based on the molecular speed ratio, s, which is the relative speed divided by the gas species most probable speed. A speed ratio greater than 5 describes the flow as a collimated beam of molecules (hyperthermal flow), and the frontal area is most significantly impacted. A speed ratio less than 5 requires the inclusion of thermal motion and its impact on all satellite surfaces (hypothermal flow). Over the extent of the thermosphere/exosphere both conditions may require consideration with hyperthermal flow at lower altitudes and hypothermal flow at higher altitudes.

The momentum flux of the reflected or re-emitted gas can be described by a number of scattering models and depends on the gas properties, the surface properties, and the angle of incidence. Specular and diffuse (or cosine) reflection represent two extremes in the spectrum of possible scattering behaviors. In describing the re-emission of an incident particle, a specular re-emission is one where the angle of the re-emitted particle equals the angle of incidence and the kinetic energy of the particle is conserved, also described as an elastic collision. A diffuse re-emission is normally associated with one where the surface adsorbs the incident molecules; these molecules equilibrate thermally with the surface and are then re-emitted with a random distribution of speed and direction associated with the temperature of the surface. This process is a form of inelastic collision where the diffusely reflected molecules are completely accommodated to the surface temperature before being re-emitted. A number of more complex scattering models are able to represent behavior spanning from specular to diffuse and have been applied to the computation of aerodynamic forces on satellites. These include Schamberg's model for quasi-specular reflection (Pilinski & Argrow, 2013) as well as versions of the drifting Maxwellian distribution such as the Cercignani Lampis Lord (CLL) model (Walker et al., 2014). These models represent the distribution of scattered velocities as a "scattering lobe" of variable width centered on either a sub-specular (closer to the surface normal direction), specular, or super-specular (closer to the surface tangent direction) vector. For a flat plate facing into the flow, a more specular reflection with kinetic energy conserved produces the greatest change in momentum and thus will increase the drag on the spacecraft over a diffuse reflection. However, for a flat plate parallel to the flow, a more diffuse scattering will produce the greatest change in momentum exchange as specular reflection results in a zero change of tangential momentum.

A thermal accommodation coefficient, α, is often used to allow for a range of energy exchanges between the gas and the surface. An $\alpha = 1$ is fully accommodated with the re-emitted molecule having a temperature equal to the surface, and an $\alpha = 0$ is one where the reflected molecule maintains its original temperature, i.e. kinetic energy is conserved upon reflection. An additional but related element to the re-emitted direction and accommodation of the incident molecules is adsorption. Adsorption is the process by which satellite surfaces become covered by atmospheric molecules that are trapped close to the surface. In this case, where the atoms "stick" to the surface for a duration exceeding the time of a gas-surface collision, the incident molecules interact with the gas adsorbate, resulting in a more diffuse and fully accommodating quality. In cases where the incident molecule interacts with the surface material and only partial accommodation occurs, the scattering can become less diffuse. Due to the surface contamination caused by adsorption, more energy is lost to the surface by incident molecules on impact. The effects of adsorption are a broader angular distribution of re-emitted molecules, which is closer to the diffuse case, and a higher accommodation of the incident molecules to the surface (Moe & Moe, 2005). These effects generally lead to an overall decrease in the drag coefficient.

Both continuum (atmospheric dynamics) and free molecular flow regimes (atmosphere-spacecraft interactions) are required to address upper atmosphere drag. Much more research is necessary in upper atmosphere flow and gas-surface interactions to adequately predict, at the necessary levels of fidelity, the actual effects on LEO objects. It will be common throughout the next sections of the chapter to move in and out of these flow regimes when describing upper atmosphere behavior and gas-surface interactions on LEO objects. It is important to consider the approach of treating the upper atmosphere gas description separately from the physics associated with determining the drag coefficient. To facilitate the discussion, the LEO drag environment will be segmented into two altitude regimes: a lower register from approximately 100–500 km altitude and an upper register from approximately 500–1000 km. The lower register represents a region where most thermosphere measurements have been made, external influences deposit their energy, atmospheric drag is the dominant nongravitational force with high accommodation, the thermosphere gas transitions to predominantly atomic oxygen (as shown in Figure 5.2), and the thermosphere gas is well represented by using continuum gas dynamics. The upper register represents a region where the most populous LEO resident space objects reside, atmospheric drag and radiation pressure compete in magnitude (though drag forces cause far more uncertainty), gas-surface interactions tend towards lower accommodation coefficients and possibly less diffuse scattering, the thermosphere gas is transitioning to an exosphere where particle motions take on ballistic trajectories, the gas composition transitions to predominantly helium and hydrogen, plasma density becomes more important, and much fewer measurements of the gas properties are available. Segmenting by geocentric altitude is favorable for identifying LEO domains but not for describing the thermosphere gas, whose more natural vertical coordinate is pressure. However, this is a common issue when discussing atmospheric drag as several different coordinate systems are often employed to represent instrument frames, observing frames, and model frames, and some caution is required when combining all elements in the satellite drag problem.

5.4. THE LOWER REGISTER (100–500 KM ALTITUDE)

5.4.1. Rarefied Gas Dynamics

In this lower register, continuum mixed gas dynamics applies for describing the mass, momentum, and energy conservation of the thermosphere. Numerical models solving these equations typically produce gas properties including mass density, composition, mass-averaged wind, and mean temperature on a 3-D global grid and short time steps (TIEGCM, CTIPe, GITM). Here, sufficient collisions between gaseous species regularly take place over represented scale lengths, i.e. low Kn, that these macroscopic properties can be determined and applied to describe gas behavior. This statistical approach involves integrations over velocity space of Boltzmann's equation. The procedure of multiplying the species velocity distribution function by powers of velocity and then integrating over all velocities is called taking velocity moments (Bittencourt, 2004). Taking higher-order velocity moments leads to the constitutive equations of mass continuity, momentum, and energy as well as higher-order moment equations. Closure of the equations can only be achieved through approximation, where the higher-order equations are expressed in terms of lower-order macroscopic properties. The transport equations for the thermospheric gas are generally known as the Navier-Stokes equations in continuous gas dynamics. This form of continuum gas dynamics is applicable if the velocity distribution function can be closely approximated by a Maxwellian and if the higher-order moment equations describing the momentum flux tensor and thermal flux tensor are expressed in terms of temperature, mass density, and wind (i.e. lower-order macroscopic variables). In other words, the momentum flux tensor is described by pressure along its diagonal and by viscosity, or stress tensor, for its off-diagonal terms. The thermal flux tensor is reduced to the heat conduction equation. This is an example of the closure issue in taking moments of the Boltzmann equation and setting approximations (see Schunk & Nagy, 2009).

The Navier-Stokes equations form the foundations for many of the global circulation models used by the upper atmosphere community to describe the behavior of the thermosphere in the lower register. In most of these models, the natural coordinate system is latitude and longitude, with pressure (or log pressure) as the vertical component (GITM is the exception using geopotential height for its vertical component). In pressure coordinates, geopotential height is a 4-D variable described by the three coordinate components and time. Geopotential height is used in description of the upper atmosphere to reduce the complexity of describing gravitational forces on a gas in a pressure coordinate system and to simplify numerical solutions. Geopotential height will deviate by a few percentage points from geocentric height as distance from the surface increases. However, geopotential height will vary appreciably on a pressure surface, and consequently the upper bound of the lower register (defined here as 500 km) will experience a range of pressure surfaces depending on the temperature and compositional makeup of the gas. Only in a very deep solar minimum will the continuum mechanics approximation be called into question near this upper boundary. Thus, much research has been applied to these models in order to describe the thermospheric gas within this lower register. A LEO object in circular orbit propagated through the model output will experience a range of pressure levels in a single orbit and, to first order, those levels will also have varying mass density, winds, and constitutive species' mixing ratios.

The lower bound of this register is marked by the mesopause, around 100 km, using the temperature gradient as a thermal fiducial, but this region can be identified dynamically as the location where turbulent mixing of the gas (eddy diffusion) equals the molecular diffusion, i.e. the turbopause. This description proves to be more relevant as turbulent mixing is highly influential on the distribution of mass density throughout the vertical column. Strong mixing processes force the variety of species to remain well mixed below the turbopause, i.e. a fixed mixing ratio similar to that observed in the lower atmosphere. The mixing results in a uniform scale height for all species that are not chemically active and is dictated by the local temperature and mean molecular weight of the gas mixture. Above the turbopause, the more efficient molecular diffusion process will work to separate individual species, each having a scale height described by their own molecular weight. However, several factors are at play that can impact a species seeking to reach diffusive equilibrium after experiencing the turbopause. One is that each species has its own turbopause height and the other is that the turbopause height can change depending on the momentum flux divergence of wave activity in the region. A change in height of the turbopause alters the number density of an individual species at the altitude by which it begins to experience molecular diffusion. This means that a light species undergoing turbulent mixing (light is defined as having a molecular weight less than the mean molecular weight of the surrounding gas composition), such as atomic oxygen or helium, will change faster with height in the turbulent mixing region than if it were allowed to diffuse on its own in that region (oxygen is also influenced by chemistry near this boundary so a more complex distribution results). Once molecular diffusion takes over at a higher altitude, the lighter species concentration has already decreased more significantly than if the turbopause action occurred at a lower altitude. The opposite process occurs with a heavy species, such as argon, where the species changes more slowly with height through the turbopause region. This leads to more argon at higher altitudes if the turbopause were to extend to a higher altitude.

Another effect that challenges molecular diffusion above the turbopause, and also effects the columnar mass density, is mixing caused by 3-D thermospheric circulations within the multiconstituent gas (Fuller-Rowell, 1998). This process can be effective in altitudes of 100–250 km where the time constant for circulation mixing can be competitive with molecular diffusion. Indeed, this is reflected in the time delays for the effects of energy inputs by different solar indices captured by the JB2008 model and described in section 5.6. Circulation processes seek to maintain mass conservation in the system, resulting in vertical and horizontal transport of mass throughout the thermosphere. Under this condition, a vertical wind in a multiconstituent gas is described as the mass-average wind needed to produce the vertical mass flux that satisfies the horizontal mass flux created in regions of divergent/convergent motion. It does not explicitly describe the behavior of individual species but only the mean mass motion of the gas, which is closely represented by the local major species. Species in the region whose molecular weight deviates from the mean molecular weight of the gas mixture results in a species distribution that differs from major gas behavior. For instance, in the lower thermosphere the vertical mass flux is dictated by the majority species, i.e. molecular nitrogen. As mass density decreases with height, the mass-averaged vertical wind must increase with height to conserve mass. The maintenance of mass conservation in the presence of vertical flows causes an adjustment process in the gas pressure so that the gas maintains hydrostasis. The major gas in the region then behaves closely to its own diffusive equilibrium. However, other species, particularly minor species in the region that, by definition, are not involved in maintaining hydrostatic equilibrium, demonstrate behavior that can deviate significantly from diffusive equilibrium. Corollary to turbopause action, vertical motions due to circulation result in vertical structure that deviates from diffusive equilibrium. The amount of deviation differs by species, and that difference depends on their molecular weight relative to the local mean molecular weight of the multiconstituent gas in the region. Species lighter than the mean molecular weight, such as helium, will experience a steeper change in concentration with height in a region of mass-averaged, upward vertical winds, and a shallower change in concentration with height in a region of downward winds, compared to its distribution under a purely molecular diffusion process. The opposite response occurs for species that are heavier than the mean molecular weight.

Essentially, upward circulations try to remix the non-major gas species, i.e. oppose molecular diffusion, so that all species follow the scale height of the mass-averaged mixture. Downward circulations work to separate non-major gas species, i.e. enhance molecular diffusion, so that species separate more efficiently. The variation in mean molecular weight with height in the lower register is nonlinear and tends to follow the transition from molecular nitrogen to atomic oxygen. Consequently, the response of each species to 3-D motion and molecular diffusion within the multiconstituent gas will vary throughout the lower register. The process of molecular diffusion increases with decreasing collision frequency, such that, in the upper portions of the lower register the species will finally reach diffusive equilibrium. However, as at the turbopause, the species concentration in the upper register will depend on its starting concentration at the lower altitude where molecular diffusion begins to dominate over circulation. This boundary lies somewhere in the middle of the lower register and is surely a dynamic and extended domain that is presently not well defined. These competitive processes of turbulence, circulation, and molecular diffusion are very much at play through most of the lower register. The processes are altitude dependent and strongly affect the mixing ratio of species through the column and the overall mass density experienced by a satellite.

Summary of the remaining issues in rarefied gas dynamics in the lower register:

- Turbopause height with location, season, year, and species
- 3-D thermosphere circulation globally beyond climatology
- Thermosphere temperature and composition distribution globally with height.

5.4.2. Gas-Surface Interactions

For gas-surface interactions (GSI), free molecular flow is a valid assumption throughout most of the thermosphere when considering most spacecraft; very large spacecraft in the lower thermosphere and vehicles at reentry altitudes <~120 km altitude must consider continuum-rarefied transitional flow regimes when assessing spaceflight dynamics (e.g. Turansky & Argrow, 2014). Here, free molecular flow will be assumed and gas-surface interactions will be applied from a kinetic point of view where the momentum and energy exchange between gaseous molecules/atoms and satellite surfaces must be evaluated at the microscopic level. The inherent assumption is that the impinging gas molecules/atoms interact with the surface before interacting with emitted molecules/atoms, thus allowing the impinging population to be evaluated independently from the outgoing population.

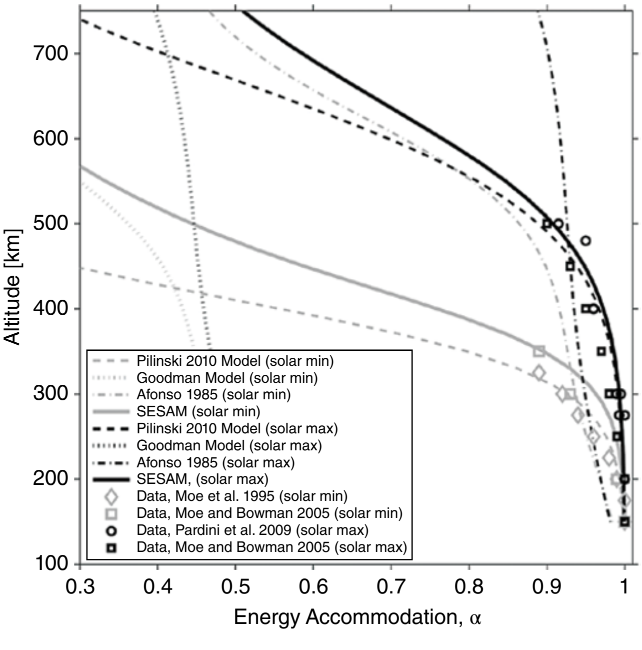

Figure 5.6 Various methods of estimating energy accommodation compared with SESAM (Source: Pilinski et al., 2013. Reproduced with permission of American Institute of Aeronautics and Astronautics, Inc.)

The description and observation of GSI in the lower register has been most developed given the availability of measurements and objects for analysis at altitudes below 500 km (Bowman & Moe, 2005; Moe & Moe, 2005; Moe et al., 1995). Pardini et al. (2010) has further evaluated physical drag coefficients for solar maximum conditions in this lower register. Pilinski et al. (2010, 2013) extended this work by developing an energy accommodation model, called the Semi-Empirical Satellite Accommodation Model (SESAM), that is consistent with the physical accommodation estimates while being applied to all levels of solar activity. Figure 5.6, from Pilinski et al. (2013), shows the energy accommodation values for LEO satellites along with SESAM (solid grey and black lines) and several other models.

This approach enables the computation of drag coefficients for changing solar activity and altitudes for spacecraft in low-eccentricity orbits. Estimates of the drag coefficients are further complicated by spacecraft geometries. Commonly, a panel method is applied to represent satellite geometries. In general, the panel method consists of the application of aerodynamic relations, such as Sentman's equations (Sentman, 1961a, 1961b), assuming diffuse scattering and a range of energy accommodation coefficients, to simplified geometries constructed from multiple panels with different orientations. A limited number of flat panels describe the entire structure of the satellite. Normal vectors and areas of each panel provide individual drag coefficients for each panel, and then a weighted sum is performed to achieve the net drag coefficient (Pilinski & Argrow, 2013). The energy accommodation coefficient has been introduced in Sentman's equation, and consequently in the panel method, by Moe et al. (2004) and Sutton (2009) as well as Doornbos (2011) for accelerometer data processing. However, the inability to model multiple reflections and shadowing effects introduces systematic errors for more complex geometries, for example the CHAMP and GRACE satellites.

Pilinski et al. (2011) and more recently Mehta et al. (2017), and references therein, have developed sophisticated numerical techniques to physically model the drag coefficient for satellites with complex geometries. They applied those techniques to the CHAMP and GRACE satellites using test particle Monte Carlo schemes (Mehta et al., 2014) and found sensitivities to gas-surface interactions and complex geometries can cause an average bias of 14%–18% for CHAMP and 10%–24% for GRACE satellites. March et al. (2019) has also addressed the complex geometry issue and has applied direct simulation Monte Carlo techniques (Bird, 1994) to CHAMP, GRACE, GOCE, and SWARM satellites resulting in more consistent density data among the four satellite missions.

Central to these studies is the manner by which the energy accommodation coefficient is estimated. In this lower register, atomic oxygen is a significant portion of the total density and a dominant species in the surface adsorption process. Adsorption, whereby monoatomic layers of gaseous atoms form on satellite surfaces, facilitates the accommodation of impinging atoms. Upon impact, the atom may maintain its kinetic energy ($\alpha = 0$), take on the temperature of the surface ($\alpha = 1$), or take some value in between. For altitudes below 500 km, the adsorbed atomic oxygen shields the incoming flow from surface properties, resulting in a GSI with high energy accommodation ($\alpha > 0.85$) and a re-emission process that is largely diffuse, essentially the Sentman model. This combination of interaction processes typically results in a surface drag coefficient that is lower than if kinetic energy were conserved upon reflection ($\alpha = 0$). The speed ratio in this lower register is often greater than 5, making the flow hyperthermal and resulting in the frontal surfaces of the spacecraft to be the dominant contributor to the overall spacecraft drag coefficient (Cook, 1965); however, elongated spacecraft and contraction of the thermosphere can reduce the speed ratio in the lower register.

Summary of the remaining issues in gas-surface interactions in the lower register:

- Modeling of spacecraft geometries and analytic versus computational methods of drag coefficients
- Assessing forces and torques on spacecraft to extract density and winds (accelerometers, GNSS tracking, radar tracking)
- Assessing errors in energy accommodation and scattering properties

5.5. THE UPPER REGISTER (500–1000 KM)

The starting altitude of the upper register at 500 km can be identified by the gas Knudsen number exceeding 1. As shown in Figure 5.4, this occurrence is defined to be the transition from the thermosphere to the exosphere. This transition is more gradual, but 500 km is a reasonable altitude to consider the start of such a transition. A correlated, and more observable transition, is the altitude by which helium and oxygen concentrations become equal. O/He transition dynamics are very important in affecting the total mass density of the LEO space environment and gas-surface interactions. The altitude of the He/O transition is lowest in solar minimum, occurring around 500 km. This is illustrated in Figure 5.7 in terms of partial pressures for each of the main species of the thermosphere for both solar maximum and solar minimum. This transition will prove useful in the discussion of rarefied gas behavior in sections 5.5.1 and 5.5.2. Typically, LEO is defined up to 2000 km, but here a limit is placed on the upper register description to 1000 km, as the neutral gas and drag behavior above this altitude is poorly known.

Other starting altitudes could be chosen for the upper register based on different considerations. For example, a common altitude threshold used in LEO deorbiting schemes concerned with orbital debris is 650 km altitude (FCC, 2018). Satellites deployed below 650 km will typically re-enter Earth's atmosphere within 25 years, even absent of any propulsive or other special deorbit capabilities. Thus, the collision risks presented by such satellites are generally lower, even if the satellites fail on-orbit and are unable to perform any active deorbiting maneuvers. Above this approximate 650 km threshold, a satellite that is not actively deorbited will remain in orbit for significantly longer periods of time. Satellites in this higher orbit require propulsive deorbit capabilities, but those missions may involve greater risk from an orbital debris perspective due to the possibility of a satellite failure that

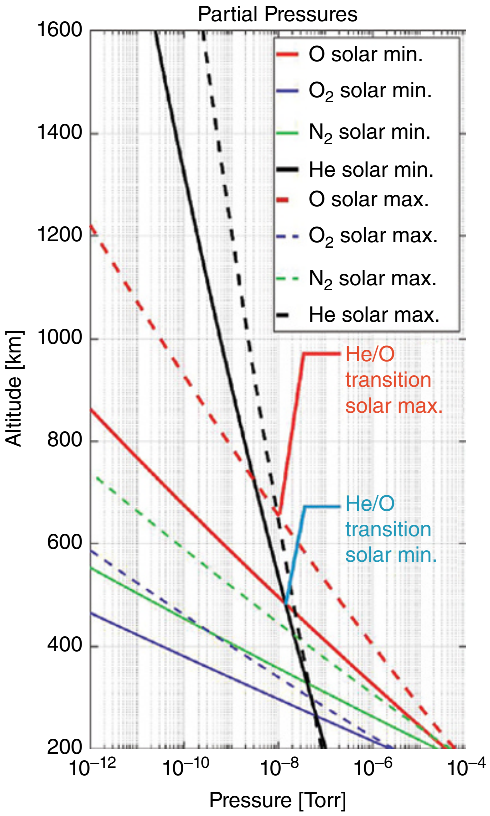

Figure 5.7 Partial pressures for thermosphere species as determined by MSIS.

can leave objects residing in LEO for much longer than 25 years. The most populous geocentric altitude range for LEO satellites and debris lies between 600 and 900 km. Many of the planned megasatellite constellations are targeting this upper register and require significant planning for deorbiting, as well as contingency plans for failed satellites that cannot be actively deorbited and other mission-generated debris.

5.5.1. Rarefied Gas Dynamics

In this upper register, failure to meet the conditions for Navier-Stokes flow requires more sophisticated descriptions and a greater expansion of terms. An example of this behavior is in transitioning through the exobase where gas velocity distributions begin to deviate more significantly from assumed near-Maxwellian behavior. Deviations from Maxwellian behavior can be accommodated by taking higher-order velocity moments, but that level of sophistication quickly creates challenges in providing sufficient descriptions. This leads to kinetic theory/Monte Carlo approaches, which have parallels to the free molecular flow descriptions used for gas-surface interactions. Here, collisional processes that describe gas behavior in the lower register give way to collision-less processes, leading to ballistic trajectories and gaseous escape as light and thermally energized species are able to overcome gravity. Inherently, the lighter and more thermally energetic species of atomic oxygen, helium, and hydrogen occupy this domain, but their relative concentrations and behavior are impacted by lower-register dynamics. The processes from below and above alter the manner by which the species change with altitude. Consequently, the total mass density can vary appreciably in regions of gas species transitions under different geophysical conditions. A particular example given here is the dynamic behavior of the oxygen/helium transition in the upper register.

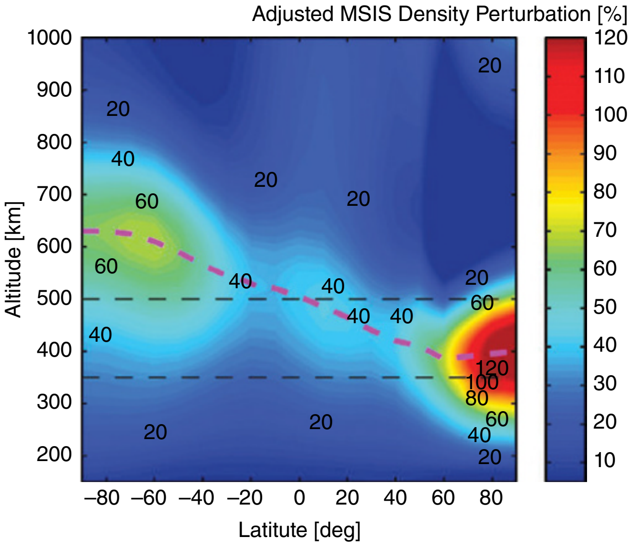

Figure 5.8 Altitudinal and latitudinal variations in mass density change during the 5–6 December 2008 geomagnetic storm estimated by MSIS after CHAMP and GRACE data adjustment. The black dashed lines represent the CHAMP and GRACE altitudes at that time. The pink dashed line indicates the maximum change in mass density and corresponds closely to where oxygen and helium have the same concentration. (Source: Liu et al., 2014. Reproduced with permission of John Wiley & Sons.)

The thermosphere-neutral constituents redistribute with altitude and latitude during geomagnetic activity in different ways that depend on the severity of the storm and the relative concentrations and molecular weights of the species that make up the multiconstituent gas. Much research has been dedicated to studying the behavior of the O/N_2 ratio during geomagnetic storms (e.g. Fuller-Rowell et al., 1990; Prölss, 1976; Rishbeth et al., 1985) in the lower register. Only recently has it been demonstrated that the helium/oxygen transition can dominate changes in mass density in the upper register during active geomagnetic times (e.g. Liu et al., 2014; Thayer et al., 2012). Furthermore, helium behavior will play a critical role in describing mass density structure and changes for altitudes extending above the thermosphere (Sutton et al., 2015).

While a major species in this upper register, helium behaves as a minor species in the lower register. This is an important distinction because a minor species may distribute itself in nonintuitive ways since, by definition, it is minor to the overall description of the gas. The description of the gas is determined by the major species that are required to follow the rules established by the constitutive equations; a minor species does not provide feedback to the major species. One well-known example that was actually revealed through spacecraft orbital behavior in the 1960s is the existence of the winter hemisphere helium bulge. In the cold and contracted winter thermosphere, helium abundance is found to be 5–10 times greater than in the summer hemisphere. This has been proven to be caused by major gas circulations imposed to satisfy mass conservation with the minor helium species responding to this circulation to form the wintertime helium bulge. The helium bulge creates an increase in mass density that can be easily detected by LEO spacecraft orbital behavior. Recently Bruinsma and Forbes (2010) and Thayer et al. (2012) revealed the winter helium bulge in GRACE data. The phenomenon has even been detected on Mars by the Maven mission (Elrod et al., 2017). For CHAMP no evidence of such behavior was detected, as CHAMP's altitude was about 150 km below GRACE, leaving it in an oxygen-rich environment. Consequently, GRACE during the solar minimum period 2008–2010 was subject to oxygen and helium composition changes along the orbit and mass density structures that deviated from diffusive equilibrium.

Upon the occurrence of a geomagnetic storm, composition and mass density changes occur. Figure 5.8 is an indication of how mass density can change with altitude during a geomagnetic storm. The black dashed line indicates the altitudes for the GRACE and CHAMP satellites in December 2008. The dashed pink line indicates where helium and oxygen are nearly equal in concentration. The mass density response to geomagnetic activity is the combined influence of variations in temperature and composition change. The altitude structure produced in Figure 5.8 is due to the different manner by which oxygen and helium respond to geomagnetic activity. This leads to a complex response at GRACE altitudes due to the dynamics of the helium/oxygen transition region. The density perturbation from quiet to active conditions is positive for all latitudes, indicating the mass density increases from quiet to active conditions, as expected, but with significant variability with latitude and altitude in the amount of change. From the summer hemisphere through the equatorial region, mass density perturbations at GRACE altitudes exceed those at CHAMP altitudes. This is indicative of mostly temperature influencing the response with little composition change as it remains primarily oxygen over this latitude region. Northward of about 40°N, the perturbation in mass density at GRACE altitudes increases less than at lower latitudes and less than at CHAMP altitudes. This response is indicative of composition change offsetting the temperature, resulting in the density perturbation in the winter hemisphere being less than that in the summer hemisphere at GRACE altitudes. In the winter polar region at GRACE altitudes, helium concentrations dominate during geomagnetic quiet times, while oxygen dominates during geomagnetic active times, which makes the mean molecular weight change significant in this region.

The mass density change with altitude maximizes near the altitude where oxygen and helium have the same concentration. This transition region is indicated by the pink dashed line in the figure. Above that altitude, the mass density change is suppressed as helium and oxygen dynamics lead to competing processes affecting the mass density: helium by transport and oxygen by thermal expansion. This is a very climatological view of the mass density change and much more investigation is required. The above description illustrates the tradeoff between temperature and mean molecular weight changes, such that the corresponding density perturbation due to geomagnetic storm varies with latitude and altitude. Note that besides temperature and mean molecular weight change, the change in the vertical gradient of mean molecular weight can also modify the density response to a geomagnetic storm, as described by Thayer et al. (2012). Thus, understanding the dynamics of oxygen and helium are paramount to understanding mass density change in this upper register. Temperature does play a role in determining how rapid the composition changes with altitude (as can be seen when contrasting altitude changes between southern summer mass density change and northern winter mass density change), as well as in how their relative scale heights change during geomagnetic activity. However, helium is strongly tied to transport processes, and this can have unexpected effects on composition and mass density distribution. The extreme solar minimum conditions accentuate this effect as the atmosphere is more contracted, and thus, transition regions occur over shorter altitude ranges and have greater variability. Under less extreme conditions, this transition region would be several hundred kilometers higher in altitude but still quite dynamic.

There remain many challenges in specifying the neutral state in this upper register. At greater altitudes, helium and hydrogen become the major species and plasma densities begin to approach those of the neutral species. Investigators have come to rely on the climatological empirical model of MSIS to provide composition information of the upper thermosphere. However, almost all of the measurements that define MSIS come from the lower register and are extrapolated to the upper register assuming diffusive equilibrium. Very little data are available to justify how high this approximation holds. Fundamental questions pervade the most basic properties of species relative concentrations, species global distribution, plasma properties, and behavior during geomagnetic activity.

The plasma environment in this region is equally challenging and strongly coupled to the neutral gas as charge exchange processes dominate. Furthermore, effects on satellite drag due to the plasma environment become an added complication for these altitudes. Plasma ion composition in the upper register measured by incoherent scatter radars and satellites show the pressing need for updated studies of topside mass-resolved plasma concentrations, and these can yield indirect information on neutral helium behavior. In particular, helium ions are dynamic and can reach more than 50% of total ion populations at solar maximum (Bailey & Sellek, 1990; Gonzalez et al., 2004; Heelis et al., 1990), reflecting the variations of neutral helium itself. Craven et al. (1995) noted that observed He+ from the Atmosphere Explorer spacecraft were lower than modeled predictions by over a factor of 2 in a wide range of conditions, a difference that was ascribed to fundamental uncertainty in the neutral helium concentration. Further observations of upper register He+ combined with modeling studies remain

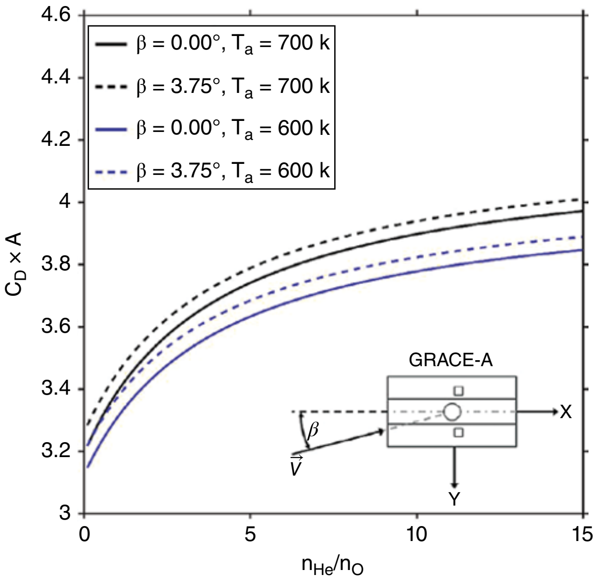

Figure 5.9 GRACE-A panel model C_DxA as a function of He/O ratio at two values of atmospheric temperature and angle of attack (β). (Source: Thayer et al., 2012. Reproduced with permission of John Wiley & Sons.)

extremely valuable, as they can derive important indirect information on neutral helium through correct interhemispheric plasma transport modeling (e.g. Lie-Svendsen et al., 1992) using CTIP-e, TIE-GCM, and other advanced models.

Summary of the remaining issues in rarefied gas dynamics in the upper register:

- Lower register specification of thermosphere gas
- Composition behavior in oxygen, helium, and hydrogen
- Physics-based simulations of thermosphere-exosphere transitions
- Exosphere gas dynamics
- Plasma environment

5.5.2. Gas-Surface Interactions

The description of gas-surface interactions becomes acutely more uncertain in this upper register as the gas becomes more tenuous, changes in gas composition occur, and the drag force weakens to where solar radiation pressure, Earth-reflected solar radiation pressure, and IR-emitted Earth radiation pressure must also be included in order to isolate the influence of atmospheric drag. The adsorbed atomic oxygen surface coverage on spacecraft surfaces along with the associated changes in energy accommodation become strongly altitude dependent in this upper register, further complicating the description of drag (Pilinski et al., 2010, 2013). Pardini et al. (2006) demonstrate the variability for a single drag coefficient model caused by changes in the ambient environment and solar conditions. The discrepancies between various aerodynamics models, caused largely by a variety of GSI assumptions within those models, is as big as the whole range of C_D values predicted by some of the C_D models and is largest in the exospheric region above 500 km. Note also that aerodynamic models such as the Semi-Empirical Satellite Accommodation Model are constrained by aerodynamic data but that this data has thus far been limited to altitudes below approximately 500 km (Pilinski et al., 2013). The discrepancies in atmospheric neutral densities between various atmospheric models computed along the paths of two satellites flying at 800 km and 600 km can reach as much as 100%. It has long been understood that a significant number of these model discrepancies are caused by assumptions made about satellite drag coefficients during the construction of those models.

Effectively, both adsorbed surface coverage and energy accommodation decrease as the molar mass decreases, and this occurs with increasing altitude. An upper altitude threshold postulated to maintain near full accommodation and diffuse emission is about 700 km during solar maximum conditions (Moe & Bowman, 2005; Pardini et al., 2010). In these instances, analytic approaches to determine the drag coefficient, such as by Sentman (1961a), have been applied at these altitudes and below. This altitude will be even lower under solar minimum conditions. Above that altitude, the surface contamination decreases, the energy accommodation coefficients decrease, and the angular distribution of reemitted molecules may have an increasingly important quasi-specular component (Saltsburg et al., 1967). Furthermore, the flow becomes more hypothermal as the speed ratio decreases, requiring the inclusion of thermal motion of the impinging gas in the analysis. All of these effects lead to an increase in the drag coefficient with height, but little observational data are available to evaluate these processes sufficiently.

A change in thermosphere composition from the chemically reactive and heavier atomic oxygen to the inert and much lighter helium impacts the drag coefficient. Figure 5.9 illustrates this point by computing the drag coefficient: the area product for the GRACE-A satellite using the Sentman (1961a) model, which assumes near-full accommodation and diffuse re-emission. This analysis was to evaluate the presence of helium during the deep solar minimum of 2008 at GRACE altitudes near 479 km. During this period, the MSIS model was performing poorly and a sensitivity test of different exospheric temperatures and He/O ratios was employed to assess their impact on the drag coefficient. An increase in the amount of helium relative to oxygen increases the drag coefficient for a given temperature. This is due to a decrease in the speed ratio as the most probable thermal speed increases with the presence of a lighter species. The lower speed ratio causes more atoms to reach the long side of the satellite and increase the momentum exchange between the spacecraft and the atmosphere. An increase in He/O ratio from 5 to 10 increased the drag coefficient by about 20%. An increase in temperature also produces an increase in the drag coefficient again associated with a decrease in the speed ratio.

A spacecraft with elongated surfaces in a low-eccentricity orbit, such as GRACE, in the upper register can experience significant changes in its drag coefficient within a single orbit due to varying composition structure. As described in section 5.5.1, for solstice conditions, the winter high latitudes are inundated with helium while oxygen dominates in the summer high latitudes. A change in He/O from less than 1 in the summer hemisphere to more than 50 in the winter hemisphere is possible within a single orbit (e.g. Liu et al., 2014). Thus, one quarter of its orbit will experience a change in drag coefficient that, if not properly accounted for, would introduce a bias in retrieving mass density. Poor representation of composition and temperature in the upper register, in addition to the changing conditions of gas-surface interactions, can therefore limit the accuracy of physically modeled drag coefficients.

A further consideration is the role of charged aerodynamics in the upper register. Here, plasma concentrations approach neutral concentrations, creating a direct plasma-surface interaction effect that can rival neutral gas-surface interactions. Furthermore, a greater susceptibility to spacecraft charging at these altitudes creates greater potentials and introduces an indirect interaction due to field effects. Recent research into plasma effects on satellite drag has been performed by Capon et al. (2018, 2019). The approach taken was to construct a surrogate model to describe the variation of a charged drag coefficient with plasma-scaling parameters to assess its contribution to the overall drag coefficient for LEO objects. This remains a challenging topic and one that will require further evaluation to determine its overall impact on drag.

Summary of the remaining issues in gas-surface interactions in the upper register:

- Introduction of charge drag
- Changes in adsorption and accommodation factors
- Transitions from diffuse to near-specular scattering
- Effects of composition change on drag coefficient modeling

5.6. SOLAR AND GEOMAGNETIC DRIVERS

As mentioned in the introduction to this chaper, the variability in atmospheric neutral density, especially due to space weather events, is the primary error source for LEO objects. Thus, improved estimates of atmospheric density positively impacts the operations and performance of critical space assets. In this section, the most significant advances in the last 40 years related to the improvement of density specification resulting from solar and geomagnetic drivers to empirical models, i.e. the kinds that are still used in operations, are described.

First, note that the primary energy input to the thermosphere are solar irradiances, especially in the extreme ultraviolet (EUV) wavelength range ($10 \le \lambda < 121$ nm), but also extending energetically into the soft X-ray ($0.1 \le \lambda < 10$ nm) and hard X-ray ($0.001 \le \lambda < 0.1$ nm) bands as well as less energetically into the Lyman-α (121. nm) and far ultraviolet (FUV) ($122 \le \lambda < 200$ nm). These photons are directly absorbed by neutral atoms and molecules resulting in dissociation or ionization. Secondary energy inputs are Joule heating (frictional heating with respect to the neutral atmosphere) and electron precipitation that excites atomic and molecular species (1–10 eV) as well as ionizes the neutrals (0.01–10 keV).

Drivers to thermosphere models use solar irradiances, indices, or proxies as well as geomagnetic indices or proxies. It is important to clarify that proxies and indices are not the same, as identified by the ISO standard for determining solar irradiances (IS 21348). Specifically, a solar irradiance proxy is a measured or modeled surrogate for solar spectral irradiances at specified wavelengths or over a wavelength bandpass, i.e. it may be only empirically related. A solar irradiance index, on the other hand, is a measured or modeled indicator, i.e. expresses an activity level, of actual solar irradiances at specific wavelengths or over a wavelength bandpass. The same is true for a geomagnetic activity index or proxy.

Thus, for physics-based thermospheric density models, solar spectral irradiances themselves are used. Common bandpasses are 1 nm bins or 37 wavelength bins and groups (Hinteregger et al., 1981). Geomagnetic drivers, such as the electron or ion fluxes, are input with an energy spectrum to characterize particle precipitation. Electric fields can be modeled or measured as an important method for characterizing Joule heating.

However, for empirical models, solar and geomagnetic indices or proxies are used to parameterize those energy inputs. This is because empirical models have historically been faster and more efficient to run in operational centers. For example, the $F_{10.7}$ and Ap proxies described below have been used extensively as solar and geomagnetic energy inputs, with their legacies extending back to the 1960s. In this section of the chapter, we describe more useful indices and proxies that have been developed since the early 2000s to better characterize solar inputs and the evolution of geomagnetic storms. For solar energy inputs, it is desirable to have solar indices and proxies that vary differently through time. This strategy of using multiple solar indices has significantly improved the accuracy of density modeling. These are also summarized in the ISO International Standard on Earth upper atmosphere (IS 14222:2013).

5.6.1. Legacy Drivers ($F_{10.7}$ and Ap)

Paetzold (1960) discovered that his analysis of solar data from a 20-cm antenna failed in the summer because of moisture condensation in the antenna. However, he noted that the 10-cm antenna in Ottawa did not have a moisture problem. Thus, using the data from the Ottawa 10-cm antenna, Paetzold discovered annual and semiannual variations in density as determined from early satellite drag data. Jacchia (1965, 1971) used this information to develop correlations with the 10.7-cm solar radio flux, $F_{10.7}$ to define the basis for thermospheric temperatures, which have an effect on densities. Thus, while the 10.7 cm measurements ($F_{10.7}$) are measured on the ground, i.e. the signal is not absorbed by the atmosphere, he found a good proxy for the solar irradiances absorbed in the thermosphere.

Jacchia used $F_{10.7}$ to represent all solar energy that was available for thermospheric heating, and it came to be thought of as an EUV proxy. Thermospheric heating is dominated by the solar chromospheric EUV energy, but it additionally comes from coronal soft X-ray, Lyman-α, and photospheric FUV wavelengths (Banks & Kockarts, 1973).

Geomagnetic activity for empirical models has been represented by the Ap index, which reports planetary geomagnetic amplitude activity (Mayaud, 1980). It is translated from the Kp geomagnetic index that is derived from geomagnetic field measurements made at locations around the world. Official ap values are calculated at the GeoForschungsZentrum Potsdam Adolf-Schmidt-Observatory for Geomagnetism in Germany, where the daily Ap is obtained by averaging the eight 3-hour values of ap for each day. The U.S. Air Force Weather Agency (AFWA) also calculates an estimated ap from a different, smaller set of stations than used for calculating the official ap values. The AFWA ap values are available through products issued by NOAA Space Weather Prediction Center. Daily Ap and 3-hour ap indices were used in early satellite orbit analysis because the time scales of geomagnetically induced variability they represented were consistent with the variations in satellite drag–derived densities (Moe, 1966; Moe & Nebergall, 1969).

5.6.2. Contemporary Drivers (S_{10}, M_{10}, Y_{10}, Dst)

The use of other indices to represent complex thermospheric heating processes has evolved over the years. A range of solar irradiances in a variety of spectral bands emanate from different solar atmosphere layers; all these photons are absorbed by various atomic and molecular species at unique unit optical depth layers in the terrestrial atmosphere. Schmidtke (1976) first postulated developing multiple solar indices to improve thermospheric density models. Tobiska (1988) then applied this concept using both Lyman-α and $F_{10.7}$ to represent chromospheric and coronal solar emissions. This methodology was extended to the development of the JB2006 model (Bowman, Tobiska, Marcos, & Valladares, 2008) using three separate solar indices to map these complex solar irradiances to thermospheric optical depths. JB2008 (Bowman, Tobiska, Marcos, Huang, et al., 2008) further extended this methodology to include an additional solar temperature region (the hot corona) and an additional thermospheric layer, i.e. the 85–100 km mesopause and lower thermosphere.

The first three indices, $F_{10.7}$, $S_{10.7}$, $M_{10.7}$ (Tobiska et al., 2008) were combined with a fourth index, $Y_{10.7}$. Collectively, these were adopted as part of the COSPAR International Reference Atmosphere (CIRA) 2014. It was the ability to insert more physics into thermospheric density drivers in the form of specific solar wavelengths linked to optical depths that enabled JB2008 to substantially reduce thermospheric densities' variation uncertainties (Bowman, Tobiska, Marcos, Huang, et al., 2008; Marcos et al., 2006; Tobiska et al., 2008).

5.6.3. $F_{10.7}$ Proxy

$F_{10.7}$ was first measured by Covington (1948) on a daily basis beginning 14 February 1947. At the present time, the 10.7 cm solar radio flux is measured at the Dominion Radio Astrophysical Observatory (DRAO) in Penticton, British Columbia, by the Solar Radio Monitoring Programme, which is operated jointly by the National Research Council (http://www.nrc-cnrc.gc.ca) and the Canadian Space Agency. Observations of the $F_{10.7}$ flux density values are made at 17, 20, and 23 UTC each day, then processed and transmitted to users automatically (see the DRAO website, https://nrc.canada.ca/node/1101). The 20 UTC observed values (not 1 AU) are archived at the World Data Center and used for the JB2008 historical inputs. The physical units of $F_{10.7}$ are $\times 10^{-22}$ W m^{-2} Hz^{-1} and their numerical value is customarily used without the multiplier, being called solar flux units (sfu). In other words, a 10.7 cm solar radio emission of 150×10^{-22} W m^{-2} Hz^{-1} is simply referred to as $F_{10.7} = 150$ sfu.

$F_{10.7}$ is a useful proxy for the combination of chromospheric, transition region, and coronal solar EUV emissions modulated by bright solar active regions whose energies at Earth are deposited in the thermosphere. Because of the high EUV– $F_{10.7}$ correlation, Jacchia developed empirical equations for exospheric temperatures that varied with solar activity and that could be used in atmospheric density models, e.g. CIRA72 (COSPAR, 1972). $F_{10.7}$ does not actually interact with the Earth's (or other planetary) atmosphere, i.e. the radiation can be measured all the way to the Earth's surface. It originates mostly in the solar cool (low) corona by electrons in thermal free-free (bremsstrahlung) emission in the vicinity of sunspots and in widely distributed areas associated with the hot complexes of solar activity (Tapping & DeTracey, 1990). The dependence on few processes, combined with its localized formation in the cool corona, i.e. a region that is closely coupled with magnetic structures responsible for creating the XUV–EUV irradiances, makes this a good generalized solar proxy for thermospheric heating.

The running 81-day centered smoothed $F_{10.7}$ values, using the moving boxcar method, are referred to as F_{81}. The observed archival daily $F_{10.7}$ values and their 81-day running center-smoothed values, F_{81}, with a 1-day lag are shown in Figure 5.10 and are described in other work (Bowman, Tobiska, Marcos, Huang, et al., 2008; Bowman, Tobiska, Marcos, & Valladares, 2008). The 1-day lag had the best correlation with satellite-derived density residuals. Figure 5.10 shows the solar cycle 23 $F_{10.7}$ index from 1 January 1997 to 1 January 2009.

Linear regression is used with daily $F_{10.7}$ to scale and report all JB2008 solar indices in units of sfu. Days where there are missing data values are not included in the regressions. $F_{10.7}$ is the recognized historical EUV proxy and, by reporting other proxies or indices in sfu, it is very easy to qualitatively identify similarities and differences between them. For solar energy inputs, it is desirable to have solar indices and proxies that vary differently through time. This strategy of using multiple solar indices has significantly improved the accuracy of density modeling as reported by Bowman, Tobiska, Marcos, Huang, et al. (2008).

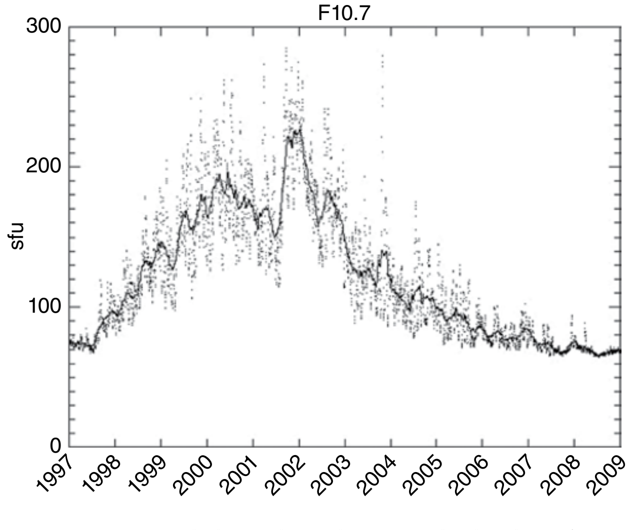

Figure 5.10 $F_{10.7}$ daily and 81-day smoothed values from 1 January 1997 to 1 January 2009.

5.6.4. $S_{10.7}$ Index

As described by Tobiska et al. (2008), the $S_{10.7}$ index is the integrated 26–34 nm solar irradiance that is measured by the Solar Extreme-Ultraviolet Monitor (SEM) instrument on the NASA/ESA Solar and Heliospheric Observatory (SOHO) research satellite. SOHO had an uninterrupted view of the Sun by operating in a halo orbit at the Lagrange Point 1 (L1) on the Earth-Sun line, approximately 1.5 million km from the Earth. SEM was built and operated by University of Southern California's Space Science Center PI team (Judge et al., 2001). SOHO was launched on 2 December 1995, and SEM has been making observations since 16 December 1995. The SEM instrument measures the 26–34 nm solar EUV emission with 15-second time resolution in this first-order broadband wavelength range.

The $S_{10.7}$ index is an activity indicator of the integrated 26–34 nm solar emission and is created by first normalizing the data, then converting it to sfu via a first-degree polynomial fit with $F_{10.7}$. Spikes from abnormal flares and missing data were excluded from the fitting vectors. Normalization is achieved for the 1 AU adjusted epoch values, denoted as SOHO_SEM26_34, by division of a mean value over a time frame common to multiple datasets. The mean value equals 1.9955×10^{10} photons cm^{-2} s^{-1}. The common time frame is 16 December 1995 to 12 June 2005, which is generally equivalent to solar cycle 23. The resulting index is called $S_{10.7}$.

In addition to this basic derivation, corrections to $S_{10.7}$ are made as follows. The originally released version of $S_{10.7}$ (v1.8) ranged from 1 January 1996 to 30 December 2005. In versions 3.0–3.9 used by JB2006, the $S_{10.7}$ values between those dates are the original ones derived in v1.8. However, in versions 3.0–3.9 and versions 4+ after 12 June 2005, a slight long-term trend was removed to ensure that similar values at the minima of solar cycles 22 and 23 were achieved. For JB2008 ($S_{10.7}$ values v4.0 and higher), a new derivation was completed as given in equation (5.3), and there may be slight differences of <0.5% compared to earlier versions of $S_{10.7}$. Figure 5.11 shows $S_{10.7}$ and the S_{81} (81-day centered smoothed) values (v4.0) for solar cycle 23 from 1 January 1997 to 1 January 2009. Daily updated values are found at the JB2008 menu link on the Space Environment Technologies (SET) website (http://spacewx.com).

$$S_{10.7} = (-2.90193) + (118.512)\left[\frac{SOHO\_SEM26\_34}{1.9955x10^{10}}\right] \tag{5.3}$$

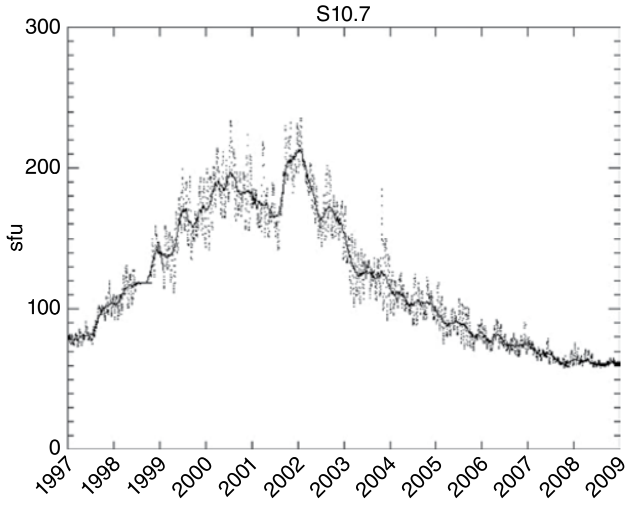

Figure 5.11 $S_{10.7}$ daily and 81-day smoothed values from 1 January 1997 to 1 January 2009.

Chromospheric He II at 30.4 nm and coronal Fe XV at 28.4 nm dominate the broadband SEM 26–34 nm irradiances, but that bandpass includes contributions from other chromospheric, transition region, and coronal lines. When the SOHO SEM and TIMED single event effect (SEE) 26–34 nm integrated data are compared, there are differences in the time series, particularly during active solar conditions. It is possible that the SOHO SEM measurements are slightly contaminated with second-order emissions from the coronal 17.1 nm Fe IX line that have not been removed; however, this topic needs further investigation. The energy in this bandpass principally comes from solar active regions, plage, and network. Once the photons reach the Earth, they are deposited (absorbed) in the terrestrial thermosphere, mostly by atomic oxygen above 200 km. The daily $S_{10.7}$ index and its 81-day running center–smoothed values, S_{81}, with a 1-day lag (the best correlation with satellite density residuals), are also described in Bowman, Tobiska, Marcos, Huang, et al. (2008). A 1-day lag is consistent with the average atomic oxygen thermal conduction timescale in the thermosphere above 180 km.

5.6.5. M10.7 Proxy

Tobiska et al. (2008) describe the development of the $M_{10.7}$ index. It is derived from the Mg II core-to-wing ratio (cwr) that originated from the NOAA series operational satellites, e.g. NOAA-16, -17, -18, which hosted the Solar Backscatter Ultraviolet (SBUV) spectrometer (Heath & Schlesinger, 1986; Viereck et al., 2001). This instrument has the objective of monitoring ozone in the Earth's lower atmosphere and, secondarily, making solar UV measurements. In its discrete operating mode, a diffuser screen is placed in front of the instrument's aperture in order to scatter solar middle ultraviolet radiation near 280 nm into the instrument. Although the NOAA data are from operational satellites, the SORCE/SOLSTICE and ERS-2/GOME research satellites also make the Mg II cwr measurements. In addition, starting with the GOES–16 satellite, Mg II cwr is also measured.

The 280 nm solar spectral band contains photospheric continuum and chromospheric line emissions. The Mg II h and k lines at 279.56 and 280.27 nm, respectively, are chromospheric in origin, while the weakly varying wings or continuum longward and shortward of the core line emission are photospheric in origin. The instruments from all satellites observe both features. On the ground, the ratio of the Mg II variable core lines to the nearly nonvarying wings is calculated. The result is mostly a measure of chromospheric solar active region emission that is theoretically independent of instrument sensitivity change through time. However, long-term changes can occur in the index if instrument wavelength calibrations change in flight or the solar incidence angle into the instrument changes. The daily Mg II cwr, described by Viereck et al. (2001), has historically been provided through the NOAA Space Weather Prediction Center (SWPC). It is likely, however, that the index values at NOAA SWPC are presently uncorrected. SET has developed and provides a corrected, operational Mg II cwr data product (MgIIcwr_SET) available at the "Products" menu link of http://spacewx.com that uses the NOAA-16, -17, -18, SORCE/SOLSTICE, and ERS-2/GOME data sources. Tobiska et al. (2008) describes the detailed processing of the MgIIcwr_SET product. The NOAA data come directly through NOAA NESDIS, and SET uses the DeLand algorithm (Cebula & DeLand, 1998; DeLand & Cebula, 1994) to create the index.

The Mg II cwr is an especially good proxy for some solar FUV and EUV emissions. It well represents photospheric and lower chromospheric solar FUV Schumann-Runge Continuum emission near 160 nm that maps into lower thermosphere heating due to O_2 photodissociation (Bowman, Tobiska, Marcos, Huang, et al., 2008). Since a 160 nm solar FUV emission photosphere index is not produced operationally, the MgIIcwr_SET proxy is used and modified into the $M_{10.7}$ index for comparison with the other solar indices. This derivation is performed in the following manner. A relationship between the long-term (multiple solar cycle) daily MgIIcwr_SET and $F_{10.7}$ is created by making a first-degree polynomial fit to produce a coefficient set that can translate the index into sfu. The result is M*10.7. Next, a correction is added for the decline of solar cycle 23 to account for NOAA 16 instrument degradation that may be related to its diffuser screen illumination geometry changing with time; this cause is

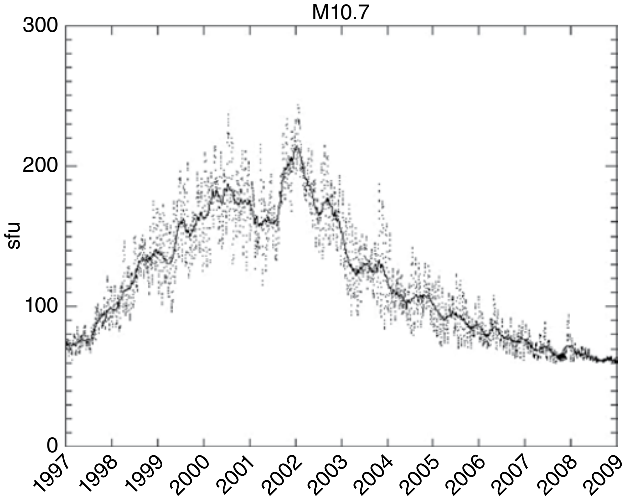

Figure 5.12 $M_{10.7}$ daily and 81-day smoothed values from 1 January 1997 to 1 January 2009.

unconfirmed. The correction is accomplished by using another first-degree polynomial fit between a trend ratio and day number starting 2448542.0 JD (12 October 1991 12:00 UT) near the peak of solar cycle 22. The trend ratio is formed from the 365-day center smoothed M*10.7 divided by the 365-day center smoothed F10.7. Equation (5.4) is the final v4.0 formulation of the $M_{10.7}$ index. The derived $M_{10.7}$ index is reported in sfu, i.e. $F_{10.7}$ units with a lower threshold minimum value set to 60. There may be slight differences of up to 1% compared to earlier versions of $M_{10.7}$.

$$M_{10.7} = \left[-2107.6186 + \left(8203.0537\right)\left(MgIIcwr\_SET\right)\right] + \left[\left(M*10.7\right)\left(1.2890589 + \left(-8.3777235x10^{-5}\right)*x - 1\right)\right] \tag{5.4}$$

The day number is $x = 0, 1, 2, \ldots$, with $x = 0$ equivalent to starting on 2448542.0 JD. Figure 5.12 shows the $M_{10.7}$ index during solar cycle 23 from 1 January 1997 to 1 January 2009. The daily $M_{10.7}$ and its 81-day running center-smoothed values, M_{81}, are shown in Figure 5.12 and are used with a 2-day lag in JB2008 as a proxy for the Schumann-Runge continuum FUV emission (Bowman, Tobiska, Marcos, Huang, et al., 2008). Originally, the JB2006 model, which did not use $Y_{10.7}$, had a lag time for $M_{10.7}$ of 5 days since the index was incorporating a combination of lag times from several energy transfer processes in the lower thermosphere to the mesopause. However, with the addition of the lower altitude (85–100 km), relevant $Y_{10.7}$ index, a shorter lag time was appropriate for $M_{10.7}$, which represents O_2 photodissociation, recombination, conduction, and transport processes at the 95–110 km level. A two-day lag is consistent with the average molecular oxygen dissociation and thermal conduction timescale in the thermosphere above 95 km, although eddy and turbulent conduction processes may play a role.

5.6.6. $Y_{10.7}$ Index

The $XL_{10.7}$ index was developed as a candidate index for the JB2006 model (Tobiska et al., 2008) but was unused. While developing the JB2008 model, it was determined that a thermospheric energy contribution to satellite drag from the 80–95 km region was significantly correlated with the composite $XL_{10.7}$ solar index.

Solar X-rays in the 0.1–0.8 nm wavelength range come from the cool and hot corona and are typically a combination of both very bright solar active region background that varies slowly (days to months) plus flares that vary rapidly (minutes to hours), respectively. The photons arriving at Earth are absorbed in the lower thermosphere to mesopause (85–100 km) by molecular oxygen (O_2) and molecular nitrogen (N_2), where they ionize those neutral constituents to create the ionospheric D-region.

The X-ray spectrometer (XRS) instrument is part of the instrument package on the GOES series operational spacecraft. The GOES/XRS provides the historical through current epoch 0.1–0.8 nm solar X-ray emission data with a 1-minute cadence and as low as 5-minute latency. These data, which are particularly useful for flare detection, are continuously reported by NOAA SWPC at their website, http://www.swpc.noaa.gov/. Tobiska and Bouwer (2005) used the GOES/XRS 0.1–0.8 nm data to develop an index of the solar X-ray active region background, without the flare component, for operational use. This is called the Xb_{10} index and is used to represent the daily energy that is deposited into the mesosphere and lower thermosphere.

While the 0.1–0.8 nm X-rays are a major energy source in these atmospheric regions during high solar activity, they relinquish their dominance to another emission that reaches the same optical depth, i.e. the competing hydrogen (H) Lyman-α emission that is the major energy source in this atmosphere region during moderate and low solar activity. Lyman-α is created in the solar upper chromosphere and transition region and demarcates the EUV from the FUV spectral regions. It is formed primarily in solar active regions, plage, and network; the photons, arriving at Earth, are absorbed in the mesosphere and lower thermosphere, where they dissociate nitric oxide (NO) and participate in water (H_2O) chemistry. Lyman-α was regularly observed by the SOLSTICE instrument on the UARS and SORCE satellites as well as by the SEE instrument on TIMED (Woods et al., 2000). Starting with the GOES–16 satellite, Lyman-α is also measured.

Since these two solar emissions are competing drivers to the mesosphere and lower thermosphere, a composite solar index of the Xb_{10} and Lyman-α was developed. It does not contain a flare component and is weighted to represent mostly Xb_{10} during solar maximum and to represent mostly Lyman-α during moderate and low solar activity. A normalized F_{81}, F_{81norm}, consisting of the 81-day centered smoothed $F_{10.7}$ divided by its mean value for the common time frame of 1 January 1991 through 16 February 2008 is used as the weighting function and multiplied with the Xb_{10} and Lyman-α (Lya) expressed as ratios to their solar maximum values. The resulting index is called $Y_{10.7}$ and equations (5.5), (5.6), and (5.7) describe this index as reported in sfu.

$$Y_{10.7} = F_{81norm}X_{10} + \left[\left(1 - F_{81norm}\right)L_{10}\right] \tag{5.5}$$

$$L_{10} = -88.3926 + \left(3.35891\times10^{-10}\,Lya\right) + \left(2.40481\times10^{-22}\,Lya2\right) \tag{5.6}$$

$$X_{10} = -42.5991 + \left(0.533669\right)Xb_{10} \tag{5.7}$$

X_{10} has a minimum threshold value of 40.

This daily index was tested with multiday lags, and the 5-day lag was found to have the strongest correlation signal in the satellite drag density residuals after modeled density variations due to the other solar indices were removed. The 81-day running center–smoothed values, Y_{81}, are also used with the 5-day lag. The 5-day lag is consistent with the average molecular oxygen and molecular nitrogen thermal conduction timescales in the lower thermosphere above 85 km, although eddy and turbulent conduction may also play a role. Figure 5.13 shows the $Y_{10.7}$ index during solar cycle 23 from 1 January 1997 to 1 January 2009.

Figure 5.14 provides a comparison between all four indices for the time frame of 1 January 1997 to 1 January 2009. The 81-day smoothed values are used to highlight the trends of each proxy or index. Figure 5.14 shows that each index or proxy captures a different type of solar energy variability. The composite of these four indices and proxies is the most complete representation to date, for empirical thermospheric density models, of the solar XUV, EUV, Lyman- α, and FUV energy that is deposited at optical depths ranging from 85 km to above 200 km. It is these energies that heat the thermosphere and affect satellite orbits. By expressing the proxies and indices in common units, their contribution to the daily density variability in the JB2008 exospheric temperature can be determined. The $F_{10.7}$ contribution to daily exospheric temperature variability is 9.8%, $S_{10.7}$ is 74.1%, $M_{10.7}$ is 10.3%, and $Y_{10.7}$ is 5.8%.

Table 5.1 provides the mapping of each index, including the data used to derive them, from its solar irradiance source(s) to the thermospheric optical depth(s) in which it is effective. The table includes the ISO 21348 spectral category, ISO 21348 spectral subcategory, wavelength range in units of nm, solar source temperature region, solar source feature, altitude region of terrestrial atmosphere absorption at unit optical depth in units of km, and terrestrial atmosphere thermal region of energy absorption. The indices and proxies that are marked with an asterisk (*) have been selected for use in the JB2008 empirical thermospheric density model and specifically in its exospheric temperature equation. Table 5.2 summarizes the characteristics of the daily solar indices including their observing facility, the instrument(s) used for observing the index/proxy, the nominal observation time frame, the measurement cadence, latency, and an assessment of the observational availability.

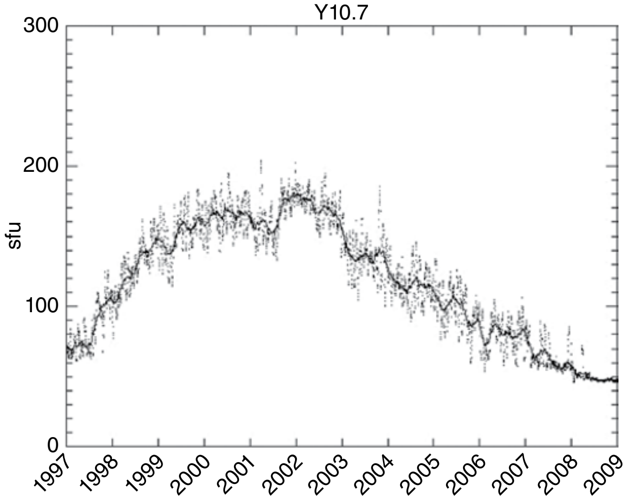

Figure 5.13 $Y_{10.7}$ daily and 81-day smoothed values from 1 January 1997 to 1 January 2009.

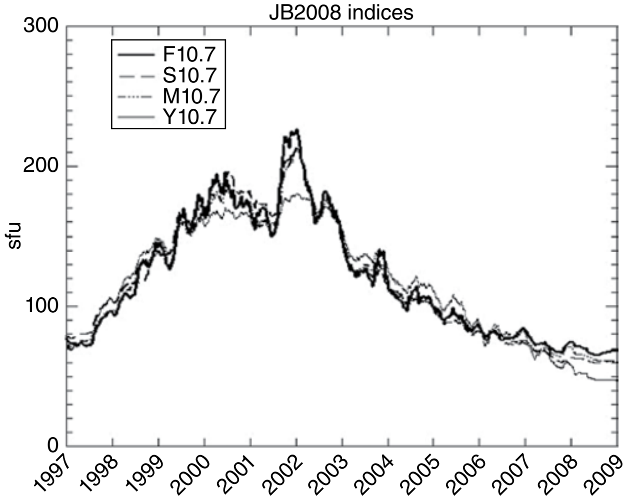

Figure 5.14 $F_{10.7}$, $S_{10.7}$, $M_{10.7}$, and $Y_{10.7}$ daily and 81-day smoothed values from 1 January 1997 to 1 January 2009.

Table 5.1 Solar indices related to atmospheric heating.

Index	IS 21348 Spectral category	IS 21348 Spectral subcategory	Wavelength range (nm)	Solar source temperature region[1]	Solar source feature[1]	Atmosphere absorption (unit optical depth, km)[2]	Terrestrial atmosphere absorption (thermal region)[2]
*$F_{10.7}$	Radio	Radio	10.7E7	Transition region, cool corona	Active region	90–500	Thermosphere with 1-day lag; 9.8% daily variability contribution
*$S_{10.7}$	UV	EUV	26–34	Chromosphere, corona	Active region, plage, network	200–300	Thermosphere with 1-day lag; 74.1% daily variability contribution
*$M_{10.7}$	UV	FUV	160	Photosphere-lower chromosphere	SRC	95–110	Lower thermosphere with 2-day lag; 10.3% daily variability contribution
$MgII_{cwr}$	UV	MUV	280[3]	Chromosphere	Active region, plage, network	200–300	Thermosphere
*$Y_{10.7}$	X-rays and UV	X-rays+H Lyman-α	0.1–0.8, 121	Chromosphere, transition region, hot corona	Active region, plage, network	85–100	Mesopause-lower thermosphere with 5-day lag; 5.8% daily variability contribution
H Lya	UV	H Lyman-α	121	Transition region, chromosphere	Active region, plage, network	85–100	Mesopause-lower thermosphere
X_{b10}	X-rays	X-rays	0.1–0.8	Hot corona	Active region background	85–100	Mesopause-lower thermosphere

* Index or proxy is used in the JB2008 model exospheric temperature equation.

[1] Vernazza et al., 1976; Vernazza et al., 1981.

[2] Banks & Kockarts (1973).

[3] The *h* and *k* lines at the band center are chromospheric and are referenced to blackbody continuum wings at edges of bandpass.

Table 5.2 Characteristics of daily JB2008 solar indices.

Index or proxy	Observing facility	Instrument	Observation time frame	Measurement cadence	Measurement latency	Operational availability
$F_{10.7}$	Penticton ground observatory	Radio telescope	1947–2009	3 times/day	Up to 24 hours	yes
$S_{10.7}$	SOHO, GOES	SEM, EUVS	1996–2009	15-second	Up to 24 hours	(a)
$M_{10.7}$	NOAA-16,17,18, SORCE, ERS-2	SBUV, SOLSTICE, GOME	1991–2009	2 times/day	Up to 24 hours	yes
$Y_{10.7}$	GOES-12, UARS, SORCE, TIMED	XRS, SOLSTICE (2), SEE	1991–2009	1-minute, 16 times/day	Up to 10 minutes, up to 48 hours	(b)

(a) SOHO/SEM is a NASA research instrument but provides daily irradiances on an operational cadence; GOES 13 EUVS B channel makes measurements in the same bandpass as SOHO SEM.

(b) GOES XRS is a NOAA operational instrument, whereas TIMED/SEE and SORCE/SOLSTICE are NASA research instruments providing daily irradiances on an operational measurement cadence.

(c) UARS/SOLSTICE stopped in 2005; SORCE/SOLSTICE intends to provide data for several years.

5.6.7. Geomagnetic Indices

The geomagnetic indices used in JB2008 incorporate existing as well as expanded empirical modeling formulations compared to previous Jacchia and MSIS-type models. A two-index formulation now captures low, unsettled, and substorm/storm-related geomagnetic activity. When the ap value is 40 and below (unsettled to quiet activity), the ap value is used. Above that threshold, the code assumes that there is a storm/substorm in progress and the Disturbance Storm Time (Dst) index is used.

The Dst index is an indicator of the strength of the storm-time ring current in the inner magnetosphere. During the main phase of geomagnetic storms, the ring current becomes highly energized and produces a southward-directed magnetic field perturbation at low latitudes on the Earth's surface. This is opposite to the normal northward-directed main field. The quick-look Dst index is calculated hourly and released through the World Data Center in Kyoto, Japan (http://swdcwww.kugi.kyoto-u.ac.jp/dst_realtime/index.html) using measurements from four off-equatorial magnetic observatories.

Dst is an "absolute" index and is reported in units of nT; magnetic observatory data are required for its calculation. Magnetic observatories are specially designed and carefully operated facilities that provide stable-baseline magnetometer data over long periods of time. Typically, an observatory supports the operation of fluxgate, proton-precession, and declination-inclination (theodolite) magnetometer systems. Sensors are situated on stable piers, and along with their acquisition electronics, they are operated in temperature-controlled conditions. Therefore, measurements from the various sensor systems can be combined to produce data that are extremely accurate. Traditionally, four stations have been used for the Dst calculation: Hermanus (HER), South Africa; Kakioka (KAK), Japan; Honolulu (HON), Hawaii; and San Juan (SJG), Puerto Rico. These stations have been continuously operated by national agencies for decades, and the data that they produce has high quality. These four stations also provide good longitudinal coverage that is needed to make a global estimation of the average ring-current intensity.

Most magnetic storms begin with sharp decreases (southward-directed negative values) in Dst, called the storm sudden commencement, in response to increased solar wind pressure. Following a southward turning of the interplanetary magnetic field, Dst decreases as ring current energy increases during the storm's main phase. During the recovery phase, the ring current energy decreases and Dst increases until the storm's end, when the magnetic field perturbation has ceased. In time series traces, Dst shows a transition from early to late recovery phases that is characterized by significant changes in the rate of change (slope). This occurs as the distribution of the ring current becomes symmetric in local time. It should be noted that a significant fraction of magnetic storms manifest more complex structuring, including multiple main and partial recovery phases.

Use of Dst as an index for the energy deposited in the thermosphere during magnetic storms is more accurate than the use of the ap index. This is because Dst has higher temporal resolution with an ability to segregate storm phases with their corresponding magnitudes. On the other hand, the 3-hour ap index is an indicator of general magnetic activity over the Earth and responds primarily to currents flowing in the ionosphere and only secondarily to magnetospheric variations. The ap index is derived from measurements by observatories at high latitudes that can be blind to energy input during large storms, and it can underestimate the effects of storms on the thermosphere.

During storm periods, the thermosphere acts as a driven-but-dissipative system where the changes in exospheric temperature change due to storm effects can be expressed by a differential equation as a function of Dst. To determine the effects on exospheric temperature, and thereby the thermospheric density distribution at any time in a storm, it is necessary to integrate the differential equation, taking into account the change in exospheric temperature while starting at the storm commencement and proceeding throughout the entire storm period. An algorithm for determining the storm events was developed (Bowman, Tobiska, Marcos, Huang, et al., 2008) that locates the temporal start, minimum, recovery slope change, and final end of the storm as reflected in the Dst index. The algorithm can incorporate the changes due to multiple or complex storms. The ap, Dst, and change in exospheric temperature values used to drive JB2008 thermospheric densities that are a result of geomagnetic activity are updated hourly and provided at the JB2008 website accessible through the JB2008 menu link at http://spacewx.com.

5.7. CONCLUSIONS

This chapter describes remaining issues in describing and predicting upper atmosphere drag on LEO spacecraft. A significant issue is providing a physical description of the LEO drag environment, and how it changes due to external influences, independently of the physical description for gas-surface interactions that determine the sensitivity of the spacecraft to a change in the upper atmosphere. The chief drivers to the atmosphere, i.e. solar and geomagnetic energy sources, are the largest factors in predicting upper atmosphere change. It has been a common approach to use LEO spacecraft orbital behavior as a means to extract space environment properties, particularly gas mass density and winds, and then reapply this description of the space environment to predict future spacecraft behavior using spacecraft orbit propagators. This approach leads to mutual coupling between spacecraft response and atmosphere change that results in convoluted uncertainties that can be challenging to quantify. Unraveling LEO spacecraft sensitivities from space environment changes requires independent gas property measurements of the space environment (particularly temperature and composition), improved physical models of the LEO drag environment to predict the response under varying external solar and geomagnetic influences, improvements in the specification of these external influences, and an independent means to measure the processes involved in gas-surface interactions.

The chapter addressed these particular issues by segmenting the LEO drag environment into a lower register of 100–500 km altitude and an upper register of 500–1000 km. The lower register represents a region where most thermosphere measurements have been made, atmospheric drag is the dominant nongravitational force with high accommodation, the thermosphere gas transitions to predominantly atomic oxygen, the solar and geomagnetic drivers are depositing their energy, and the thermosphere gas is well represented by using continuum gas dynamics. Several remaining issues for the thermosphere gas in the lower register were identified and discussed, including the need to define the turbopause height with location, season, year, and species, describe the 3-D thermosphere circulation globally beyond climatology, observe the thermosphere temperature and composition distribution with height, and describe the solar and magnetospheric energy deposition. Remaining issues in gas-surface interactions for the lower register include modeling of drag coefficients and accounting for complex geometries, identifying errors in energy accommodation and scattering properties, and translating forces and torques to extract mass density and winds.

The upper register represents a region where the most populous LEO objects reside, atmospheric drag and radiation pressure compete, gas-surface interactions are more specular and less accommodating, the thermosphere gas is transitioning to an exosphere where particle motions take on ballistic trajectories, the gas composition transitions to predominantly helium and hydrogen, plasma densities become important, and much fewer measurements of the gas properties are available. Several remaining issues for the thermosphere gas in the upper register were identified and discussed, including the need to specify the lower register of the thermosphere gas as it serves as a necessary lower boundary condition for the upper register; describe oxygen, helium, and hydrogen behavior; simulate thermosphere-exosphere transitions in gas behavior; and understand exosphere and plasmasphere behavior. Remaining issues in gas-surface interactions in the upper register include understanding the impacts of plasma on drag, describing adequately the adsorption and accommodation behavior, understanding diffuse-to-specular scatter transitions, and determining drag coefficient dependencies on composition.

Section 5.6 provided a new contribution to the literature by describing the approach used to account for the solar and geomagnetic indices that drive the JB2008 model. This model was the most significant improvement in empirical thermospheric density modeling since the 1960s and formed the basis for the dramatic improvements in the HASDM system in the 2000s.

Today, greater fidelity in space environment specification is required for LEO spacecraft operations, collision avoidance procedures, and space environment forecasting. This chapter described the processes involved and the remaining issues needing resolution in order to improve the description, prediction, and use of the LEO drag environment in a future that is looking to significantly expand LEO spacecraft operations. These remaining issues are challenging as they require many more observations and well-thought-out experiments in order to advance understanding and capability.

ACKNOWLEDGMENTS

The authors would like to acknowledge helpful discussions with John Emmert, Tim Fuller-Rowell, Matt Hejduk, David Vallado, and Eelco Doornbos. This work was partially supported by University of Colorado's Grand Challenge initiative in the Space Weather Technology, Research, and Education Center, NSF CEDAR Award No. AGS 1452309. Section 5.6 was partially supported by SPAWAR contracts N6600118P7815 and N6600119P6237.

REFERENCES

Bailey, G. J., & Sellek, R. (1990). A mathematical model of the earth's plasmasphere and its application in a study of He+ at L=3. *Ann. Geophys.*, *8*, 171.

Banks, P., & Kockarts, G. (1973). *Aeronomy*. New York: Academic Press.

Bird, G. A. (1994). Molecular gas dynamics and the direct simulation of gas flows. Oxford Engineering Science series, No. 42. Oxford: Clarenden Press.

Bittencourt, J. A. (2004). *Fundamentals of plasma physics*, 3rd ed. Springer-Verlag.

Bowman, B. R., & Moe, K. (2005), Drag coefficient variability at 175–500 km from the orbit decay analyses of spheres. AAS/AIAA, Astrodynamics Specialist Conference, American Astronautical Society, Paper AAS 05-257, San Diego, CA.

Bowman, B. R., Tobiska, K. W., Marcos, F. A., Huang, C. Y., Lin, C., & Burke, W. F. (2008). A new empirical thermospheric density model JB2008 using new solar and geomagnetic indices. AIAA/AAS, Astrodynamics Specialist Conference and Exhibit 18–21 August 2008, Honolulu, Hawaii (AIAA 2008-6438).

Bowman, B. R., Tobiska, W. K., Marcos, F. A., & Valladares, C. (2008). The JB2006 empirical thermospheric density model. *J. Atm. Sol-Terr. Phys.*, *70*, 774–793.

Bruinsma, S. (2015). The DTM-2013 thermosphere model. *J. Space Weather Space Clim.*, *5*, A1. https://doi.org/10.1051/swsc/2015001

Bruinsma, S. L., & Forbes, J. M. (2010). Anomalous behavior of the thermosphere during solar minimum observed by CHAMP and GRACE. *J. Geophys. Res.*, *115*, A11323. doi:10.1029/2010JA015605

Bussy-Virat, C. D., Ridley, A. J., & Getchius, J. W. (2018). Effects of uncertainties in the atmospheric density on the probability of collision between space objects. *Space Weather*, *16*, 519–537. https://doi.org/10.1029/2017SW001705

Capon, C. J., Brown, M., & Boyce, R. R. (2018). Direct and indirect charged aerodynamic mechanisms in the ionosphere. *Adv. Space Res.*, *62*(5), 1090–1101.

Capon, C. J., Smith, B., Brown, M., Abay, R., & Boyce, R.R. (2019). Effect of ionospheric drag on atmospheric density estimation and orbit prediction. *Adv. Space Res.*, *63*, f2495–2505. DOI: 10.1016/j.asr.2019.01.013

Cebula, R. P., & DeLand, M.T. (1998). Comparisons of the NOAA-11 SBUV/2, UARS SOL- STICE, and UARS SUSIM Mg II solar activity proxy indexes. *Solar Phys.*, *177*, 117– 132.

Cook, G. E. (1965). Satellite drag coefficients. *Planet. Space Sci.*, *13*, 929–946.

COSPAR (1972). International Reference Atmosphere. Compiled by the COSPAR Working Group IV. Amsterdam: North-Holland Publishing.

Covington, A. E. (1948). Solar noise observations on 10.7 centimeters. *Proc. of the I.R.E.*, *36*, 454.

Craven, P. D., Comfort, R. H., Richards, P. G., & Grebowsky, J. M. (1995). Comparisons of modeled N+, O+, H+, and He+ in the midlatitude ionosphere with mean densities and temperatures from Atmosphere Explorer. *J. Geophys. Res.*, *100*(A1), 257– 268. doi:10.1029/94JA02306

DeLand, M. T., & Cebula R. P. (1994). Comparisons of the Mg II index products from the NOAA-9 and NOAA-11 SBUV/2 instruments. *Solar Phys.*, *152*, 61–68.

Doornbos, E. (2011). Thermospheric density and wind determination from satellite dynamics (Ph.D. thesis). Delft University of Technology. ISBN: 978-90-9026051-8.

Doornbos, E., van den IJssel, J., Luehr, H., Foerster, M., Koppenwallner, G., Bruinsma, S., et al. (2010). Neutral density and crosswind determination from arbitrarily oriented multiaxis accelerometers on satellites. *J. Spacecraft Rockets*, *47*, 580–589. https://doi.org/10.2514/1.48114

Elrod, M. K., Bougher, S., Bell, J., Mahaffy, P. R., Benna, M., Stone, S., et al. (2017). He bulge revealed: He and CO2 diurnal and seasonal variations in the upper atmosphere of Mars as detected by MAVEN NGIMS. *J. Geophys. Res. Space Physics*, *122*. doi:10.1002/2016JA023482

Emmert, J. T., Picone, J. M., & Meier, R. R. (2008). Thermospheric global average density trends, 1967–2007, derived from orbits of 5000 near-Earth objects. *Geophys. Res. Lett. 5*, 35. https://doi.org/10.1029/2007GL032809

Emmert, J. T. (2015). Thermospheric mass density: A review. *Advances in Space Research*, *56*(5), 773–824.

FCC (2018). Mitigation of orbital debris in the new space age (IB Docket No. 18-313).

Fuller-Rowell, T. J. (1998). The “thermospheric spoon”: A mechanism for the semiannual density variation. *J. Geophys. Res.*, *103*(A3), 3951– 3956. doi:10.1029/97JA03335

Fuller-Rowell, T. J., Rees, D., Quegan, S., Moffett, R. J., Codrescu, M. V., & Millward, G. H. (1996). A coupled thermosphere-ionosphere model (CTIM). In R. W. Schunk (Ed.), *Handbook of ionospheric models* (pp. 217–238). Logan, Utah: Utah State Univ.

Fuller-Rowell, T., Rees D., Tinsley B., Rishbeth H., Rodger A., & Quegan S. (1990). Modelling the response of the thermosphere and ionosphere to geomagnetic storms: Effects of a mid-latitude heat source. *Advances in Space Research*, *10*(6), 215–223.

Gaposchkin, E. M., & Coster, A. J. (1988). Analysis of satellite drag. *The Lincoln Laboratory Journal*, *1*, 203–224.

González, S. A., Sulzer, M. P., Nicolls, M. J., & Kerr, R. B. (2004). Solar cycle variability of nighttime topside helium ion concentrations over Arecibo. *J. Geophys. Res.*, *109*, A07302. doi:10.1029/2003JA010100

He, C. Y., Yang, B., Carter, E., Kerra, S., Wu, F., Deleflie, H., et al. (2018). Review and comparison of empirical thermospheric mass density models. *Progress in Aerospace Sciences*, *103*, 31–51.

Heath, D. F., & Schlesinger, B. M. (1986). The Mg 280-nm doublet as a monitor of changes in solar ultraviolet irradiance. *J. Geophys. Res.*, *91*, 8672–8682.

Heelis, R. A., Hanson, W. B., & Bailey, G. J. (1990). Distributions of He+ at middle and equatorial latitudes during solar maximum. *J. Geophys. Res.*, *95*, 10313.

Hejduk, M. D., & Snow, D. E. (2018). The effect of neutral density estimation errors on satellite conjunction of the upper atmosphere. *Space Weather*. https://doi.org/10.1029/2017SW001720

Hinteregger, H. E., Fukui, K., & Gilson, B. R. (1981). Observational, reference and model data on solar EUV, from measurements on AE-E. *Geophys. Res. Lett.*, *8*, 1147.

Hoots, F. R., & Roehrich, R. L. (1980). Spacetrack Report #3: Models for Propagation of the NORAD Element Sets. U.S. Air Force Aerospace Defense Command, Colorado Springs, CO.

International Standards Organization (2013). IS 14222. Space environment (natural and artificial) – Earth upper atmosphere. Geneva.

International Standards Organization (2007). IS 21348. Space environment (natural and artificial) – Process for determining solar irradiances. Geneva.

Jacchia, L. G. (1965). Static diffusion models of the upper atmosphere with empirical temperature profiles. *Smithsonian Contr. Astrophys.*, *8*, 215. Smithsonian Institution Astrophysical Observatory.

Jacchia, L. G. (1971). Revised static models of the atmosphere and exosphere with empirical temperature profiles. *Smithsonian Astrophys. Special Report 332*, Smithsonian Institution Astrophysical Observatory.

Jacchia, L. G. (1977). Thermospheric temperature, density, and composition: New models. *Special Report 375*. Smithsonian Institution Astrophysical Observatory.

Judge, D. L., Ogawa, H. S., McMullin, D. R., Gangopadhyay, P., & Pap, J. M. (2001). The SOHO CELIAS/SEM EUV Database from SC23 Minimum to the Present. *Adv. Space Res.*, *29*(12), 1963.

King-Hele, D. G., & Quinn, E. (1965). The variation of upper-atmosphere density between sunspot maximum (1957-8) and minimum (1964). *J. Atmos. Terr. Phys.*, *27*, 197–209.

Klinkrad, H. (2017). Large satellite constellations and related challenges for space debris mitigation. *The Journal of Space Safety Engineering*, *4*, 59–60. http://dx.doi.org/10.1016/j.jsse.2017.06.002

Lie-Svendsen, O., Rees, M. H., & Stamnes, K. (1992). Helium escape from the Earth's atmosphere: The charge exchange mechanism revisited. *Planet. Space Sci.*, *40*, 1639.

Liu, X., Thayer, J. P., Burns, A., Wang, W., & Sutton, E. (2014). Altitude variations in the thermosphere mass density response to geomagnetic activity during the recent solar minimum. *J. Geophys. Res. Space Physics*, *119*. doi:10.1002/2013JA019453

March, G., Doornbos, E. N., & Visser, P. N. (2019). High-fidelity geometry models for improving the consistency of CHAMP, GRACE, GOCE and Swarm thermospheric density data sets. *Adv. Space Res.*, *63*(1), 213–238.

Marcos, F. A., Bowman, B. R., & Sheehan, R. E. (2006). Accuracy of Earth's thermospheric neutral density models, AIAA 2006-6167, AIAA/AAS Astrodynamics Specialist Conference, Keystone, CO, August.

Marcos, F. A., Kendra, M. J., Griffin, J. M., Bass, J. N., Larson, D. R., & Liu, J. J. (1998). Precision low Earth orbit determination using atmospheric density calibration. *J. Astronaut. Sci.*, *46*(4), 395–409.

Mayaud, P. N. (1980). Derivation, meaning, and use of geomagnetic indices. *Geophysical Monograph 22*. Washington, DC: American Geophysical Union.

Mehta, P. M., & Linares, R. (2017). A methodology for reduced order modeling and calibration of the upper atmosphere. *Space Weather*, *15*(10), 1270–1287.

Mehta, P. M., Walker, A., Lawrence, E., Linares, R., Higdon, D., & Koller, J. (2014). Modeling satellite drag coefficients with response surfaces. *Adv. Space Res.*, *54*(8), 1590–1607. doi:10.1016/j.asr.2014.06.033

Mehta, P. M., Walker, A. C., Sutton, E. K., & Godinez, H. C. (2017). New density estimates derived using accelerometers on board the CHAMP and GRACE satellites. *Space Weather*, *15*, 558–576. doi:10.1002/2016SW001562

Moe, K. (1966). Absolute atmospheric densities determined from the spin and orbital decays of Explorer VI. *Planet. Space Sci.*, *14*, 1065–1075.

Moe, K., & Bowman, B. R. (2005). The effects of surface composition and treatment on drag coefficients of spherical satellites (AAS05-258). AAS/AIAA Astrodynamics Conference. South Lake Tahoe, California, USA.

Moe, K., & Moe M. M. (2005). Gas-surface interactions and satellite drag coefficients. *Planet. Space Sci.*, *53*, 793–801. doi:10.1016/j.pss.2005.03.005

Moe, K., Moe, M. M., & Rice, C. J. (2004). Simultaneous analysis of multiinstrument satellite measurements of atmospheric density. *J. Spacecraft Rockets*, *41*(5), 849–853.

Moe, K., & Nebergall D. (1969). Variation of geomagnetic disturbance with latitude. *J. Geo- phys. Res.*, *74*, 1305–1307.

Moe, M. M., Wallace, S. D., & Moe, K. (1995). Recommended drag coefficients for aeronomic satellites. The upper mesosphere and lower thermosphere: A review of experiment and theory. In R. M. Johnson & T. L. Killeen (Eds.), *Geophysical Monograph, Vol. 87* (pp. 349–445), Washington, DC: American Geophysical Union.

Paetzold, H.-K. (1960). COSPAR Space Research, Nice.

Pardini, C., Anselmo, L., Moe, K., & Moe, M. M. (2010). Drag and energy accommodation coefficients during sunspot maximum, *45*, (5), 638–650. https://doi.org/10.1016/j.asr.2009.08.034

Pardini, C., Tobiska, W. K., & Anselmo, L. (2006). Analysis of the orbital decay of spherical satellites using different solar flux proxies and atmospheric density models. *Advances in Space Research*, *37*(2), 392–400. https://doi.org/10.1016/j.asr.2004.10.009

Picone, J. M. Hedin, A. E., Drob, D. P., & Aikin, A. C. (2002). NRLMSISE-00 empirical model of the atmosphere: Statistical comparisons and scientific issues. *J. Geophys. Res., Space Phys.*, https://doi.org/10.1029/2002JA009430 107(A12):SIA 15–1–SIA 15–16.

Pilinski, M. D., & Argrow, B. M. (2013). Aerodynamic analysis based on challenging minisatellite payload satellite lift-to-drag measurements. *Journal of Spacecraft and Rockets*, *50*, 1162–1170. doi:10.2514/1.A32394

Pilinski, M. D., Argrow, B. M., & Palo, S. E. (2010). Semi-empirical model for satellite energy-accommodation coefficients. *Journal of Spacecraft and Rockets*, *47*, 951–956. https://doi.org/10.2514/1.49330

Pilinski, M. D., Argrow, B. M., & Palo, S. E. (2011). Drag coefficients of satellites with concave geometries: Comparing models and observations. *Journal of Spacecraft and Rockets*, *48*, 312–325. https://doi.org/10.2514/1.50915

Pilinski, M. D., Argrow, B. M., & Palo, S. E. (2013). A semi-empirical satellite accommodation model for spherical and randomly tumbling objects. *Journal of Spacecraft and Rockets*. doi: 10.2514/1.A32348

Prieto, D. M., Graziano, B. P., & Roberts, P.C.E. (2014). Spacecraft drag modelling. *Prog. Aerosp. Sci.*, *64*, 56–65. doi:10.1016/j.paerosci.2013.09.001

Prölss, G. (1976). On explaining the negative phase of ionospheric storms. *Planetary and Space Science*, *24*(6), 607–609.

Radtke, J., Kebschull, C., & Stoll, E. (2017). Interactions of the space debris environment with mega constellations: Using the example of the OneWeb constellation. *Acta Astronautica*, *131*, 55–68.

Ren T., Miao, J., & Liu, S. (2018). Atmospheric density determination using high-accuracy satellite GPS data. *Science China Technological Sciences*, *61*, 204. doi: 10.1007/s11431-016-9096-6

Richmond, A. D., Ridley, E. C., & Roble, R. G. (1992). A thermosphere/ionosphere general circulation model with coupled electrodynamics. *Geophysical Research Letters*, *19*(6), 601. https://doi.org/10.1029/92GL00401–604

Ridley, A., Deng, Y., & Toth, G. (2006). The global ionosphere-thermosphere model. *Journal of Atmospheric and Solar-Terrestrial Physics*, *68*(8), 839–864.

Rishbeth, H., Gordon, R., Rees, D., & Fuller-Rowell, T. (1985). Modelling of thermospheric composition changes caused by a severe magnetic storm. *Planetary and Space Science*, *33*(11), 1283–1301.

Roble, R. G., Ridley, E. C., Richmond, A. D., & Dickinson, R. E. (1988). A coupled thermosphere/ionosphere general circulation model. *Geophysical Research Letters*, *15*(12), 1325. https://doi.org/10.1029/GL015i012p01325–1328

Saltsburg, H., Smith Jr. J. M., & Rogers M. (Eds.) (1967). *Fundamentals of gas-surface interactions*. New York: Academic Press.

Schmidtke, G. (1976). *Geophys. Res. Lett.*, *3*, 573.

Schunk, R., & Nagy, A. (2009). *Ionospheres: Physics, plasma physics, and chemistry*. Cambridge Atmospheric and Space Science Series, 2nd ed.

Sentman, L. (1961a). Comparison of the exact and approximate methods for predicting free molecule aerodynamic coefficients. *ARS J.*, *1*, 1576–1579.

Sentman, L. (1961b). *Free molecule flow theory and its application to the determination of aerodynamic forces (Tech. Rep. TR LMSC-448514)*. Lockheed Missile and Space Co., Sunnyvale, CA.

Storz, M. F., Bowman, B. R., Branson, M.J.I., Casali, S. J., & Tobiska, W. K. (2005). High accuracy satellite drag model (HASDM). *Adv. Space Res.*, *36*, 2497–2505. doi:10.1016/j.asr.2004.02.020

Sutton, E. K., Nerem, R. S., & Forbes, J. M. (2007), Density and winds in the thermosphere deduced from accelerometer data. *Journal of Spacecraft and Rockets*, *44*(6), 1210–1219.

Sutton, E. K. (2008). Effects of solar disturbances on the thermosphere densities and winds from CHAMP and GRACE satellite accelerometer data (Ph.D. thesis). University of Colorado at Boulder.

Sutton, E. K. (2009). Normalized force coefficients for satellites with elongated shapes. *J. Spacecraft Rockets*, *46*(1), 112–116. https://doi. org/10.2514/1.40940

Sutton, E. K., Thayer, J. P., Wang, W., Solomon, S. C., Liu, X., & Foster, B. T. (2015). A self-consistent model of helium in the thermosphere. *J. Geophys. Res. Space Physics*, *120*, doi:10.1002/2015JA021223

Tapping, K. F., & DeTracey, B. (1990). The origin of the 10.7 cm flux. *Solar Phys.*, *127*(2), 321–332.

Thayer, J. P., Liu, X., Lei, J., Pilinski, M., & Burns, A. G. (2012). The impact of helium on thermosphere mass density response to geomagnetic activity during the recent solar minimum. *J. Geophys. Res.*, *117*, A07315. doi:10.1029/2012JA017832

Tobiska, W. K. (1988). A solar extreme ultraviolet flux model (Ph.D. thesis). Department of Aerospace Engineering, University of Colorado.

Tobiska, W. K., & Bouwer S. D. (2005). Solar flare evolution model for operational users. 2005 Ionospheric Effects Symposium, ed. J.M. Goodman. JMG Associates, 76.

Tobiska, W. K., Bouwer, S. D., Bowman, B. R. (2008). The development of new solar indices for use in thermospheric density modeling. *J. Atm. Solar-Terr. Phys.*, *70*, 803–819.

Turansky, C. P., & Argrow, B. M. (2014). Rigid-body dynamics in free-molecular and transition flow. *Journal of Spacecraft and Rockets*, *51*, 239–252.

Vallado, D., Crawford, P., Hujsak, R., & Kelso, T. S. (2006). Revisiting Spacetrack Report #3, AIAA/AAS Astrodynamics Specialist Conference and Exhibit, Keystone, Colorado, 21–24 August, 2006.

van den IJssel, J., & Visser, P. (2010). Performance of GPS-based accelerometer: a simulation experiment. *Adv. Space Res.*, *45*(1), 2010.

Vernazza, J. E., Avrett, E. H., & Loeser, R. (1976). Structure of the solar chromosphere. II—The underlying photosphere and temperature-minimum region. *Astrophysical Journal Supplement Series*, *30*, 1–60.

Vernazza, J. E., Avrett, E. H., & Loeser, R. (1981). Structure of the solar chromosphere, III—Models of the EUV brightness components of the quiet-sun. *Astrophysical Journal Supplement Series*, *45*, 635–725.

Viereck, R., Puga, L., McMullin, D., Judge, D., Weber, M., & Tobiska W. K. (2001). The Mg II index: A proxy for solar EUV. *Geophys. Res. Lett.*, *28*(7), 1342.

Walker A., Mehta, P., & Koller, J. (2014). Drag coefficient model using the Cercignani–Lampis–Lord Gas–Surface Interaction Model. *Journal of Spacecraft and Rockets*, *51*, 1544–1563. https://doi.org/10.2514/1.A32677

Woods, T. N., Bailey, S., Eparvier, F., Lawrence, G., Lean, J., McClintok, B., et al. (2000). TIMED Solar EUV Experiment. *Phys. Chem. Earth*, *25*, 393–396.